RESEARCH

Unsupervised learning for geologically consistent fluid flow analysis in fractured reservoirs

Elahe Kamel Targhi[1] · Guillaume Rongier[1] · Pierre-Olivier Bruna[1] · Alexandros Daniilidis[1] · Sebastian Geiger[1]

Received: 16 February 2026 / Accepted: 18 June 2026

Abstract
Naturally fractured reservoirs are essential for subsurface energy production and storage. However, the complexity and uncertainty inherent to fracture network properties make it difficult to characterise fluid flow within them. This study presents an unsupervised machine learning workflow that constrains uncertainty by establishing a systematic link between the pressure transient response observed at the well and the underlying fracture network properties. We generate a geologically consistent ensemble of 4,850 discrete fracture networks (DFNs) and simulate pressure transient responses for the same geometries under three matrix-fracture permeability configurations. For each dataset, we group pressure derivative responses into geologically interpretable flow behaviour clusters using Dynamic Time Warping (DTW) based K-medoids clustering. The resulting cluster medoids provide representative pressure derivative responses that summarise the dominant flow regime sequence within each class. The workflow consistently identifies four stable clusters across all datasets, each characterised by a distinct and repeatable sequence of diagnostic flow regimes consistent with a bounded range of fracture network properties. Feature importance ranking and SHAP values derived from a random forest classifier show that fracture intensity, wellbore fracture length, and backbone fracture fraction provide the strongest geological controls on cluster separation and hence on the emergent diagnostic signatures. Comparing clusters across datasets shows that 64.1% of DFNs retain their cluster membership, indicating that the clustering structure is primarily controlled by DFN geometry. However, for a fixed DFN, the pressure transient response varies across matrix-fracture permeability configurations, producing systematic shifts in derivative levels and in the dominance of specific flow regimes. The representative pressure derivative responses associated with each flow behaviour cluster are therefore not identical across datasets and must be interpreted within the matrix-fracture permeability configuration. Overall, the proposed framework provides a basis to constrain geological uncertainty and prioritise high-impact parameters for data acquisition in naturally fractured reservoirs, thereby improving reservoir characterisation and decision making in the early appraisal stage.

Keywords Discrete fracture networks · Pressure transient analysis · Machine learning · Random forest · Clustering

1 Introduction

Natural fractures are frequently present in the subsurface [cf. 1, 2]. It is well understood that these fractures can form high-permeability pathways that influence heat and mass transfer in the subsurface, and hence they need to be characterised reliably for development of geothermal energy [e.g., 3], groundwater management [e.g., 4], and CO_2 sequestration projects [e.g., 5]. However, directly measuring fracture network properties that control flow and

 https://doi.org/10.1007/s10596-026-10459-w

Published online: 02 July 2026

transport is inherently difficult due to the limited resolution of seismic imaging and the sparse information provided by well logs and core data [1, 2]. This lack of information introduces uncertainties that must be propagated through static and dynamic models, as variations in fracture geometry can produce large differences in connectivity and flow behaviour [6, 7]. If these geological uncertainties are not properly accounted for, it is very challenging to reliably forecast heat and mass transfer in fractured geological formations. For example, a geothermal project in Munich, Germany, experienced early thermal breakthrough due to the presence of well-connected fractures that were not considered adequately in the reservoir model [8]. Similar challenges have also been reported for CO_2 storage projects, where a mismatch between assumed and actual fracture connectivity may lead to too much pressure buildup or early leakage [9, 10].

To better constrain fracture network properties and evaluate their impact on flow behaviour, various ensemble-based and cross-disciplinary workflows have been developed [e.g., 11–14]. These approaches integrate geological observations (e.g., from outcrops, core samples, and well logs) with dynamic reservoir data to generate geologically plausible models that reduce uncertainty. For example, the geoengineering workflow proposed by Corbett et al. [15, 16] systematically links well test responses to subsurface flow architectures, with subsequent work extending the interpretation to fracture network properties [17]. In this methodology, geological data are used to construct and calibrate reservoir models by iteratively adjusting fracture network properties until simulated pressure responses match field observations. The geoengineering workflow has been successfully applied to real-field cases to reduce uncertainty and identify the most plausible fracture model consistent with both static and dynamic data [18].

Pressure transient analysis (PTA) plays a central role in Corbett et al. [16] and Egya et al. [17] workflows by using diagnostic plots of pressure transient response and its derivatives from well tests to identify characteristic flow regimes and characterise the reservoir [19–21]. The reliability of this approach depends on the availability of analytical models capable of capturing large-scale subsurface architecture. For fractured systems, the commonly used dual-porosity model by Warren and Root [22] represents a fractured reservoir as two interacting continua: a mobile fracture domain and an immobile matrix domain. The fractures provide the primary pathways for fluid transport, while the matrix blocks act as a uniformly distributed source that provides significant storage capacity but negligible flow capacity. The inter-porosity fluid exchange between these two media results in a V-shaped dip in the pressure derivative, referred to as the V-dip. The V-dip magnitude is governed by the storativity ratio, ω, which quantifies the relative fluid capacity of the fracture network with respect to the total system storage as

$$\omega = \frac{\phi_f C_{t,f}}{\phi_f C_{t,f} + \phi_m C_{t,m}}, \tag{1}$$

where ϕ_f and ϕ_m are fracture and matrix porosities, and $C_{t,f}$ and $C_{t,m}$ are the corresponding total compressibilities (Pa^{-1}) [22]. However, the Warren and Root [22] model relies on idealised assumptions such as uniformly spaced and fully connected fractures. These simplifications lead to inaccurate predictions when compared to real-world observations, as they fail to capture the complex spatial organisation and connectivity of natural fracture networks [17].

To address the limitations of idealised analytical models, the GeoType concept introduced by Corbett et al. [23] provides a systematic way to relate geological configurations to pressure derivative responses. GeoTypes are defined as families of related pressure transient responses and their derivatives derived from synthetic well-test data within a geoengineering workflow, and capture how changes in subsurface architecture translate into repeatable sequences and durations of flow regimes [23]. Building upon the GeoType concept, recent advances in artificial intelligence and machine learning (ML) have enabled a more systematic interpretation of complex pressure transient responses. Freites et al. [24] proposed a classification framework that leverages synthetic pressure transient responses from discrete fracture networks (DFNs). Using unsupervised learning techniques, the study demonstrated that fracture intensity, connectivity, and proximity to the wellbore could be inferred directly from the pressure derivative response. However, Freites et al. [24]'s workflow relies on fracture models with limited geological constraints and overly simplified geometries (e.g., only orthogonal fracture sets), which restrict the range of fracture network properties considered relative to those commonly observed in naturally fractured reservoirs.

In this study, we establish a geologically consistent and physically interpretable workflow to assess how pressure transient responses can be used to constrain fracture network properties, identify the key geological controls on flow behaviour, and guide data acquisition and early-stage reservoir characterisation. We define a design of experiments (DoE) to systematically explore the range of fracture network properties and use GeoDFN [25] to generate a large ensemble of DFNs that satisfy geological and mechanical constraints. Pressure transient responses are then simulated using the embedded discrete fracture model (EDFM), which represents fractures explicitly and captures fracture–matrix exchange without conforming meshes [26, 27]. The same DFN geometries are evaluated under three matrix-fracture permeability configurations, allowing us to explicitly isolate the influence of fracture geometry from permeability effects. Together, this framework moves beyond the simplified or idealised fracture geometries and flow representations used in Freites et al. [24], enabling a more realistic and physically consistent characterisation of flow behaviour in fractured reservoirs. The unsupervised clustering workflow is further extended by incorporating random forest classification and SHAP analysis to identify the fracture properties that most strongly control GeoType separation, thereby indicating which attributes must be constrained to reduce interpretation non-uniqueness and to guide data acquisition. Finally, we assess whether GeoTypes provide a transferable basis for well-test interpretation when matrix and fracture permeability are uncertain by comparing the clustering results across the three datasets in terms of how individual DFNs are grouped, the fracture property ranges associated with each cluster, and the corresponding GeoTypes.

2 Methodology

Figure 1 summarises the methodology adopted in this study. The machine learning workflow is applied to each dataset independently. The resulting clusters are first analysed within each dataset and then compared across datasets. In the following, we describe each step of the methodology in detail.

2.1 Design of experiment

Fracture systems develop under mechanical and geological constraints that control their topology, connectivity and hydraulic behaviour [28, 29]. Thus, defining the key fracture network properties and their geologically consistent range is the first step in building a diverse ensemble of DFNs. Table 1 lists the key fracture network properties, their chosen distribution functions and the parameter ranges informed by outcrop and modelling studies (see [25, 30] for detailed information). Parameters marked with an asterisk in Table 1 are varied during the sampling process; all other parameters are kept fixed. The model domain is set to 1 km $\times$ 1 km for all DFNs to minimise boundary effects and capture large-scale heterogeneity [28]. At this scale, the generated fracture networks capture large-scale spatial organisation rather than near-fracture detail, consistent with the level of structural information typically available from field-scale observations and drone-based outcrop imagery [31, 32].

The resulting parameter space is explored using Latin Hypercube Sampling (LHS) [44]. To better represent both sparsely and densely fractured systems, P_{21} is sampled on a logarithmic scale. This approach accounts for the nonlinear increase in connectivity near the percolation threshold and avoids under-sampling low-intensity networks, which are particularly sensitive to small changes in fracture density [34, 35]. A total of 1000 parameter combinations are sampled, based on the stabilisation of the mean and variance of the fracture network properties varied in the DoE across increasing sampling densities (see Fig. 15 in Appendix).

The intrinsic fracture permeability, k_f, and host rock matrix permeability, k_m, are key controls on fluid flow behaviour because their absolute values and relative contrast k_f/k_m govern fluid movement, storage, and exchange between the matrix and the fracture network [22, 45–47]. For each individual fracture i, k_{f_i} (m^2) is primarily

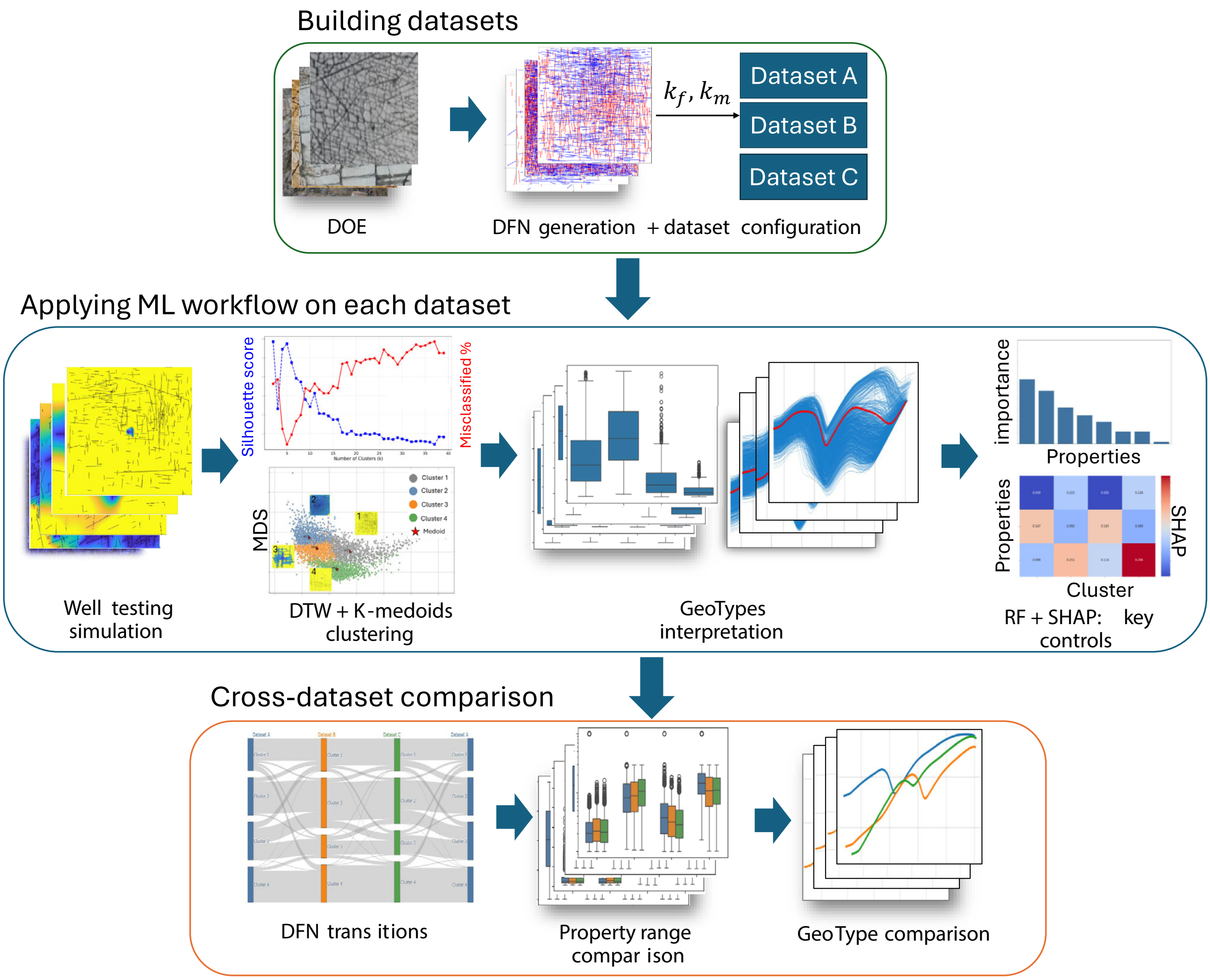

Fig. 1 Overview of the methodology used in this study to characterise fractured reservoirs using pressure transient responses

controlled by its aperture, α_i (m), and assuming parallel-plate geometry is given as [48]

$$k_{f_i} = \frac{\alpha_i^2}{12}. \tag{2}$$

For non-interacting opening-mode fractures, α_i is commonly modelled as a sub-linear function of fracture length,

$$\alpha_i = Cl_i^{0.5}, \tag{3}$$

where l_i (m) is the length of fracture i and C $(m^{0.5})$ is a pre-exponential constant that depends on the mechanical properties of the fracture and host rock [38, 49]. Alternative aperture models, including constant aperture, linear scaling, and Barton–Bandis type relationships, are discussed in Kamel Targhi et al. [25] and can all be implemented within the GeoDFN framework. The sub-linear scaling is adopted in this study to introduce controlled variability in fracture aperture across the DFN ensemble while avoiding oversimplified assumptions such as uniform aperture. The power-law exponent is kept fixed across the ensemble (0.5), because in a related study [30], where the power-law exponent was treated as a variable parameter in the DoE, it was found to strongly dominate the clustering behaviour and pressure transient response, masking the influence of other fracture network properties. Fixing the exponent therefore represents a methodological choice to isolate the effects of fracture geometry on flow behaviour, while still allowing variation in aperture and fracture permeability. For readability, the subscript i is dropped throughout the text, but aperture, length and permeability are defined individually for each fracture.

To explore how both the absolute values of k_m and k_f and their contrast k_f/k_m influence the pressure transient response, we consider two matrix permeabilities and two fracture permeability distributions. The matrix permeability is assigned either a higher value, $k_m = 10^{-14}$ m^2 (similar to sandstones [50]) or a lower value, $k_m = 10^{-16}$ m^2 (similar to tight siliciclastics [51] and volcanic units [52]). The fracture permeability is modelled using Eq. 2, and fracture apertures are computed following Eq. 3, with $C = 0.0001$ producing sub-millimetre to millimetre apertures [47, 53], and $C = 0.001$ producing apertures on the order of millimetres to centimetres, similar to macrofractures in sandstone [54] and extensional fractures in laminated carbonate units [55]. The resulting fracture permeabilities differ by roughly two orders of magnitude and generate k_f/k_m contrasts in the range 10^6 to 10^{10}, spanning mixed matrix-fracture to strongly fracture-dominated flow regimes [34, 45].

2.2 DFN generation and dataset construction

We use GeoDFN to generate a geologically consistent ensemble of DFNs. GeoDFN is an open source software that integrates statistical and mechanical rules derived from geological observations, including fracture growth constraints and stress shadow effects, to ensure geologically consistent fracture network configurations [25, 56]. As a result, if a given parameter combination is not geologically feasible, for example, leading to oversaturated networks, GeoDFN fails to generate a valid DFN. Following the GeoDFN workflow, connectivity emerges from the mechanical placement rules rather than being prescribed as an explicit input parameter, and the proportions of I, Y and X nodes (i.e. isolated fracture terminations, branching intersections, and cross-cutting intersections) are therefore not included in the DoE. We adopt a 2D representation because outcrop fracture data are typically collected from lower-dimensional horizontal pavements or vertical cliff faces, both of which provide limited exposure [cf. 57, 58].

For each parameter combination, five realisations are generated to capture stochastic variability in fracture placement. The success rate of DFN generation in this study is 97%, indicating that the selected parameter ranges (Table 1) resulted in a geologically consistent dataset of 4,850 DFNs. A subset of the generated networks is shown in Fig. 2 to illustrate the diversity of fracture patterns in the dataset.

Following DFN generation, the matrix-fracture permeability configurations defined in Table 2 are assigned to the networks to construct three datasets. These datasets share identical DFN geometries, so variations in flow behaviour within a dataset reflect only differences in the fracture network properties listed in Table 1. Across datasets, matrix-fracture permeability configurations are modified while geometry is kept fixed, enabling controlled comparison of the effects of k_m, k_f, and their contrast k_f/k_m on the fluid flow behaviour of the system.

2.3 Numerical simulation

The numerical simulation of flow and transport for the ensemble of DFNs generated in the previous step requires a modelling framework that can represent complex fracture geometries while remaining computationally efficient for simulating fluid flow in thousands of realisations. For this purpose, we use the MATLAB Reservoir Simulation Toolbox (MRST) [59, 60], an open source software that has been extensively applied for simulating a wide range of flow and transport phenomena in fractured geological formations, including solute transport [61], multiphase flow [62], upscaling [63, 64], aquifer management [65], and enhanced geothermal systems [66]. We specifically use the EDFM module in MRST. In EDFM, the matrix and fracture grids are generated independently, allowing fractures to be represented explicitly within a permeable and porous matrix without the need to generate conforming meshes, which are computationally complex and expensive. Transmissibility between fractures and the matrix, as well as between intersecting fractures, is handled through non-neighbouring connections [cf. 26, 27, 67]. This approach

https://doi.org/10.1007/s10596-026-10459-w

Table 1 Fracture parameters used for generating a comprehensive ensemble of DFNs. Asterisk (*) indicates parameters varied in the design of experiments

Parameter	Values	Explanation
Fracture intensity		Predominantly controls network permeability; higher fracture abundance increases connectivity and promotes preferential flow pathways [33].
P_{21}[a]* (m^{-1})	(0.01, 0.3)	Range chosen from inspection of the generated DFNs to effectively represent sparsely fractured networks, transitional networks near the percolation threshold [34, 35], and dense networks approaching fracture saturation, where additional fractures no longer significantly affect connectivity or flow [36].
Buffer zone		Accounts for stress shadow, a region around a fracture where new fractures are less likely to nucleate or grow because the available energy for fracture propagation is lower [29].
Method	Constant	Assuming layer-bound fractures [37].
Size (m)*	(0.5, 1.5)	Minimum spacing between fractures.
Fracture length		
Distribution	Power law[b]	Fractures are often fractal and scale invariant, and therefore their length is commonly represented by a power-law distribution [38, 39].
n (-)[b]*	(1.5, 3.5)	Controls the balance between short and long fractures and strongly influences network connectivity and flow behaviour [40].
Min / max length (m)	5 / 1000	Minimum length chosen to match the scale observable in drone imagery; maximum length limited by the model domain size.
Spatial placement		
Distribution	Poisson	Represents a statistically uniform spatial arrangement.
Min / max distance (m)	Buffer zone size / 1000	Minimum separation controlled by the stress shadow; maximum distance limited by the model domain size.
Fracture orientation		Fracture orientation, θ, is primarily controlled by the prevailing stress field during fracture formation [41].
Distribution	von Mises[c]	Circular analogue of the normal distribution and widely used for planar orientation data modelling [42].
κ[c] (-)*	(70, 120)	Varied to represent moderately to highly aligned fracture sets [43].
θ_m[c]* (°)	Set 1 = 0°; Set 2 = 60°or 90°	Two fracture sets are considered for each network. Set 1 is assigned a fixed mean orientation of 0°, while Set 2 is assigned a mean orientation of either 60° or 90° within the design of experiments. Thus, the resulting fracture networks represent either conjugate configurations (with an angle of approximately 60° between the fractures in set 1 and 2) or orthogonal configurations (with an angle of approximately 90°).
Min / max orientation (°)	$\theta_m \pm 25$	Angular spread around each mean orientation, defining the variability within each fracture set.

[a] Areal fracture intensity P_{21} is defined as $P_{21} = \sum_{i=1}^{N_f} l_i / A$, where l_i is the length of the i-th fracture, N_f is the number of fractures, and A is the domain area

[b] The power-law probability density function is $f(l) \propto l^{-n}$ where n is the length index

[c] The von Mises distribution is $f(\theta) = \exp[\kappa \cos(\theta - \theta_m)]/(2\pi I_0(\kappa))$, where θ_m is the mean direction (mean orientation), κ is the concentration parameter (orientation concentration), and I_0 is the modified Bessel function of the first kind of order zero

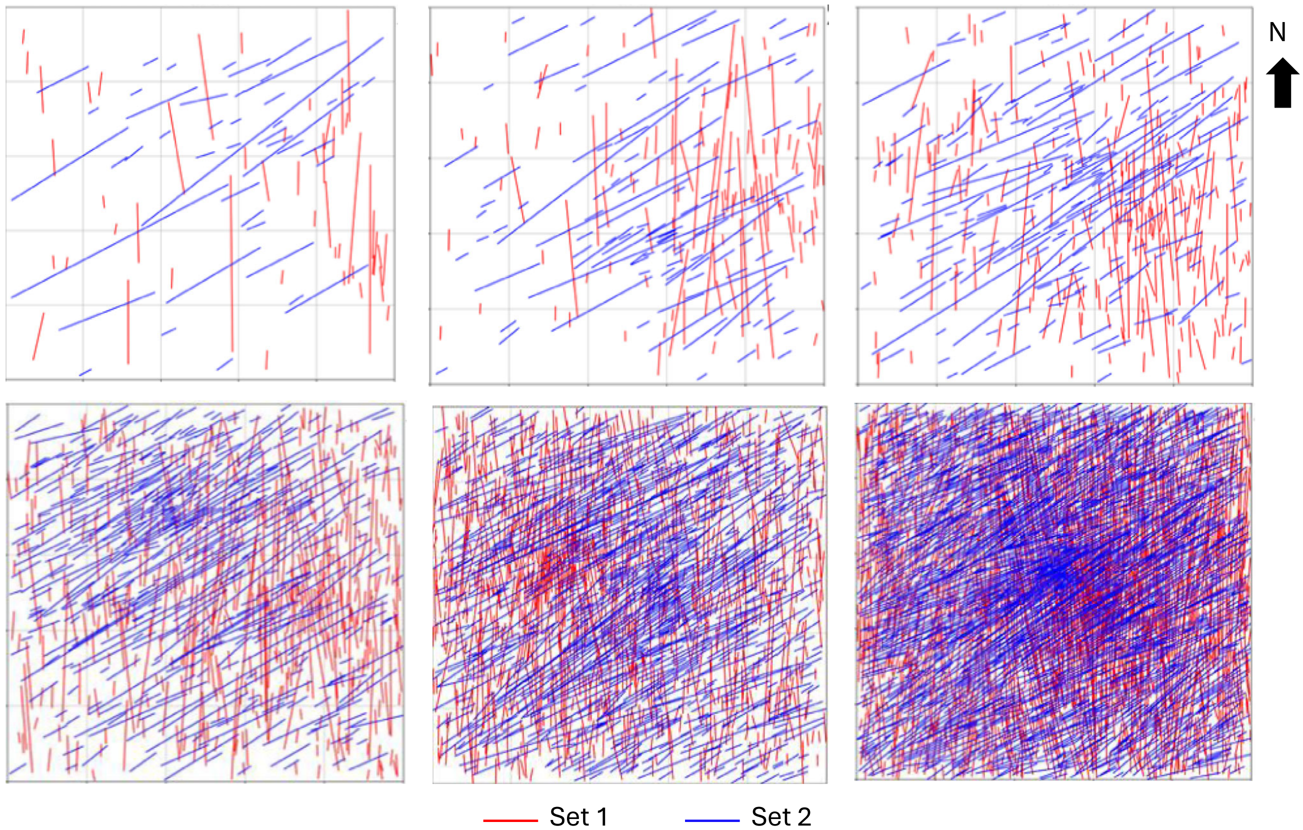

Fig. 2 Illustrative example DFNs from the full DFN ensemble shown in map view, generated by varying only P_{21} while keeping all other fracture network properties fixed. Six realisations are shown with P_{21} values logarithmically spaced between 0.01 and 0.3, illustrating the transition from sparsely to densely fractured networks

ensures that variations in fracture and matrix properties are accurately reflected in the simulated flow behaviour of the system. Fluid flow in each simulation is governed by slightly compressible single-phase flow, expressed as

$$\frac{\partial}{\partial t}(\phi_m C_r P) = \nabla \cdot \left(\frac{k_m}{\mu} \nabla P\right), \tag{4}$$

where ϕ_m is the matrix porosity, C_r is the total compressibility (Pa^{-1}), μ is the fluid viscosity (Pa s), and P is pressure (Pa).

Grid size and time-step sensitivity are assessed by progressively coarsening the spatial and temporal resolution and selecting the largest grid cell size and time step that preserve the details of the pressure transient response. The simulation domain is discretised using a uniform Cartesian grid with a cell size of 2 m$\times$ 2 m. A 2.5D (pseudo-3D) configuration is adopted by assigning a constant thickness of 10 m and extruding the fractures vertically through this thickness, while maintaining a single cell in the vertical direction. This is consistent with the assumption of

Table 2 Summary of the three datasets used to explore the influence of matrix permeability, fracture permeability and the resulting k_f/k_m contrast. All datasets share the same DFN geometries; only permeability configuration differs

Dataset	k_m (m^2)	C (m$^{0.5}$)	α (m)	k_f (m^2)	k_f/k_m
A	1×10^{-14}	0.0001	$(5 \times 10^{-4},\ 4 \times 10^{-3})$	$(2 \times 10^{-9},\ 1.33 \times 10^{-7})$	$(2 \times 10^{6},\ 1.3 \times 10^{8})$
B	1×10^{-16}	0.0001	$(5 \times 10^{-4},\ 4 \times 10^{-3})$	$(2.0 \times 10^{-9},\ 1.33 \times 10^{-7})$	$(2 \times 10^{8},\ 1.3 \times 10^{10})$
C	1×10^{-14}	0.001	$(5 \times 10^{-3},\ 4 \times 10^{-2})$	$(2.0 \times 10^{-7},\ 1.33 \times 10^{-5})$	$(2 \times 10^{8},\ 1.3 \times 10^{10})$

 https://doi.org/10.1007/s10596-026-10459-w

layer-bounded fractures, which are often sub-vertical and terminate at interfaces between different lithologies [e.g., 68, 69]. An initial time step of 10^{-6} s is used and then progressively increased by a factor of 1.1 up to 60 s. The combination of this time-stepping and grid size strategy provides sufficient resolution for reliable interpretation of the pressure transient response while keeping the computational cost tractable for thousands of simulations.

Each simulation includes a single constant-rate production well (10 m^3/day), positioned at the centre of the domain and assigned to the nearest cell intersecting a fracture. The simulations represent the drawdown period of a single-rate well test and neglect skin, wellbore storage, and superposition effects. Each run is terminated once the pressure drop in any boundary cell exceeds 0.001%, ensuring that the simulations mainly capture the transient pressure behaviour during which the pressure front propagates from the wellbore towards the boundaries. The resulting pressure transient responses are smoothed using moving averages to suppress minor numerical oscillations.

2.4 Unsupervised learning of GeoTypes from pressure curves

We then group the pressure transient responses in each dataset into clusters representing similar flow behaviour, i.e., the same sequence of flow regimes. Flow regimes refer to distinct patterns of pressure propagation and flow geometry that are diagnostic of the underlying reservoir architecture. Each regime is characterised on the log-log pressure derivative plot by a characteristic slope, M [19]. A catalogue of the flow regimes and diagnostic features observed in this study is provided in Appendix B (Table 4).

Similarity is assessed from the overall shape of the pressure derivative (P') curve, because fracture networks can exhibit the same flow behaviour while the timing of flow regime transitions and the derivative levels shift due to differences in fracture geometry and connectivity [21, 70]. We adopt the unsupervised clustering approach of Freites et al. [24], which enables systematic grouping of large pressure transient response ensembles and supports subsequent linkage to fracture network characteristics. The complete workflow is applied independently to each dataset (Datasets A to C), producing separate clustering solutions for each matrix-fracture permeability configuration (Table 2).

To quantify similarity between pressure transient responses, pairwise distances between all pressure derivative curves are computed using Dynamic Time Warping (DTW) [71, 72]. DTW is an elastic similarity measure that determines the optimal non-linear alignment between two sequences, allowing curves with similar overall shape but shifted temporal scales to be compared directly [73]. This makes DTW particularly suitable for pressure transient responses, as it enables pressure derivative curves representing the same flow regimes to be identified as similar even when the diagnostic features occur at different times. Following Freites et al. [24], DTW distances are computed using the second derivative of pressure (P'') to reduce sensitivity to vertical offsets associated with permeability scaling and to emphasise the diagnostic structure of the transient response. For each dataset, DTW is computed for all pairs of P'' curves and stored in a symmetric distance matrix, where entry (i, j) gives the DTW distance between simulations i and j.

The clustering process partitions the DTW distance matrix into k clusters using the K-Medoids algorithm [cf. 74–76]. K-Medoids is particularly suited for clustering time series data because it allows grouping data based on arbitrary dissimilarity measures, including DTW distance, and it defines each cluster centre as an actual data point in the dataset, the medoid. The medoid is the sequence that minimises the average distance to all other members of its cluster. Each medoid therefore represents an actual simulated P'' curve from the dataset (and by extension, a P' curve), and thus provides a physically interpretable reference pressure transient response that summarises the dominant fluid flow behaviour of that cluster.

To determine the number of flow behaviour clusters, clustering is first evaluated statistically across a range of cluster numbers ($k = 2$ to 40) using the silhouette score and the percentage of misclassified points [74, 77]. The silhouette score measures how well each pressure transient response is assigned to its cluster relative to neighbouring clusters. The percentage of misclassified points quantifies the fraction of responses with negative silhouette score, i.e., responses that are closer to a different cluster than to their assigned one. Three candidate cluster numbers are then selected based on local maxima in silhouette score and the corresponding local minima in the percentage of misclassified points, which indicate more coherent and better-separated clusters.

To select the optimal number of flow behaviour clusters from the candidate solutions, cluster separation and overlap are examined visually using multidimensional scaling (MDS). MDS projects the DTW distance matrix into a low-dimensional space while preserving relative dissimilarities between pressure transient responses [78, 79]. In the MDS representation, responses that plot close to each other correspond to small DTW distances and similar flow behaviour, whereas responses that plot far apart correspond to large DTW distances and dissimilar flow behaviour. A candidate cluster number is considered favourable when clusters occupy distinct regions with limited overlap, the cluster medoids are located near the centre of their assigned groups, and the medoids exhibit clearly distinguishable pressure propagation patterns. To confirm the visual interpretation, the Davies–Bouldin index [80] and the Calinski–Harabasz index [81] are computed for each candidate solution. The Davies–Bouldin index measures the average ratio of intra-cluster scatter to inter-cluster separation, with lower values indicating more compact and better-separated clusters. The Calinski–Harabasz index measures the ratio of between-cluster dispersion to within-cluster dispersion, with higher values indicating more clearly defined clusters. Together, these two metrics provide a quantitative confirmation of the visual MDS assessment and reduce reliance on visual judgement alone in selecting the optimal number of clusters. An additional interpretability check is performed by examining the representative pressure distributions of the cluster medoids at the end of the simulation, to assess whether the inferred clusters correspond to physically distinct pressure propagation patterns.

The resulting clustering for the optimum number of clusters is then confirmed by jointly examining the pressure transient responses assigned to each cluster and the fracture network property distributions of the corresponding DFNs. This step checks that responses grouped into the same cluster exhibit a similar pressure derivative behaviour and are associated with comparable ranges of fracture network properties. Different clusters are expected to show systematic differences in both the pressure derivative curves and the associated fracture network characteristics. The fracture network properties include the parameters varied in the DoE (Table 1), together with three additional metrics that influence flow behaviour: connectivity, wellbore fracture length, and the fraction of fractures belonging to the largest connected component. Connectivity is defined as the total number of fracture intersections per fracture per unit surface area. The wellbore fracture length, L_{wb}, is defined as the length of the fracture intersected by the production well. The fraction of fractures belonging to the largest connected component, f_{LCC}, is defined as

$$f_{\mathrm{LCC}} = \frac{N_{\mathrm{LCC}}}{N}, \tag{5}$$

where N is the total number of fractures and N_{LCC} is the number of fractures forming the largest connected component. To compute N_{LCC}, all fracture intersections are identified, and fractures connected directly or indirectly through one or more intersections are grouped into connected component. The largest connected component is then identified as the component containing the maximum number of fractures, which is referred to as the backbone [82].

The medoid of each identified flow behaviour cluster, i.e., the pressure transient response that minimises the average DTW distance to all other responses within the cluster, is defined as the GeoType. It serves as a physically interpretable reference pressure derivative curve that summarises the dominant sequence of flow regimes represented by the DFNs assigned to that cluster.

2.5 Diagnostic flow regime analysis of GeoTypes

The flow behaviours represented by GeoTypes are then interpreted by analysing their pressure derivative response and identifying the sequence of flow regimes they represent (Appendix B). The flow regime interpretation is examined jointly with the range of fracture network properties associated with each cluster to support geological interpretability. This allows dominant flow regime sequences to be related to characteristic ranges of fracture network properties.

This link provides a basis for using the GeoTypes during the appraisal stage of fractured reservoirs. When pressure transient data from well test are available, the measured derivative response can be compared with the GeoTypes to identify the most consistent flow behaviour cluster. Because each cluster is associated with a constrained range of fracture network properties, the matching cluster provides quantitative bounds on plausible physical characteristics. This methodology helps to reduce the non-uniqueness inherent in traditional well-test interpretation and provides a physically grounded starting point for reducing the uncertainty in fractured reservoir characterisation. The framework is developed under controlled modelling assumptions including 2D DFNs, a 2.5D fluid flow simulation, a single constant-rate well, and does not consider wellbore storage, skin, and superposition effects. In practice, operational variability and measurement noise may obscure or modify diagnostic features in the pressure derivative. The framework is therefore best interpreted as a tool for early-stage appraisal and uncertainty reduction, rather than a direct substitute for detailed well-test interpretation.

2.6 Identifying key fracture network properties controlling GeoTypes

Examining how fracture network properties vary across clusters provides an initial qualitative indication of which parameters most strongly differentiate the distinct flow behaviours identified through clustering. Properties that show systematic differences between clusters are interpreted as key fracture network properties controlling the fluid flow behaviour. In contrast, properties that remain uniformly distributed across clusters are interpreted as having limited influence on the separation of pressure transient responses, indicating that their variability does not significantly shape the observed flow regimes.

The importance of each property in distinguishing the flow behaviour clusters is further quantified by training a random forest classifier that uses the fracture network properties as inputs and the cluster labels as targets (Fig. 3). The random forest algorithm constructs an ensemble of decision trees and aggregates their predictions to improve accuracy and reduce overfitting [83]. The classifier allows new fracture networks to be assigned to the previously defined flow behaviour clusters based solely on their statistical properties. The resulting feature importance scores provide a global ranking of the parameters that most strongly discriminate between the flow behaviour clusters. To verify that the same parameters govern the classifier decisions at the level of individual predictions, SHAP (SHapley Additive exPlanations) values are computed for the trained model [84]. Unlike property distributions and feature importance, SHAP values show how each parameter value pushes an individual DFN towards a specific cluster. Together, the random forest feature importance and SHAP values identify the fracture properties that have the strongest influence on the pressure transient response of a fractured reservoir. Identifying these sensitivities supports fracture characterisation by highlighting which parameters require tighter constraints and more accurate measurement, and which can tolerate greater uncertainty without compromising the interpretation of flow behaviour.

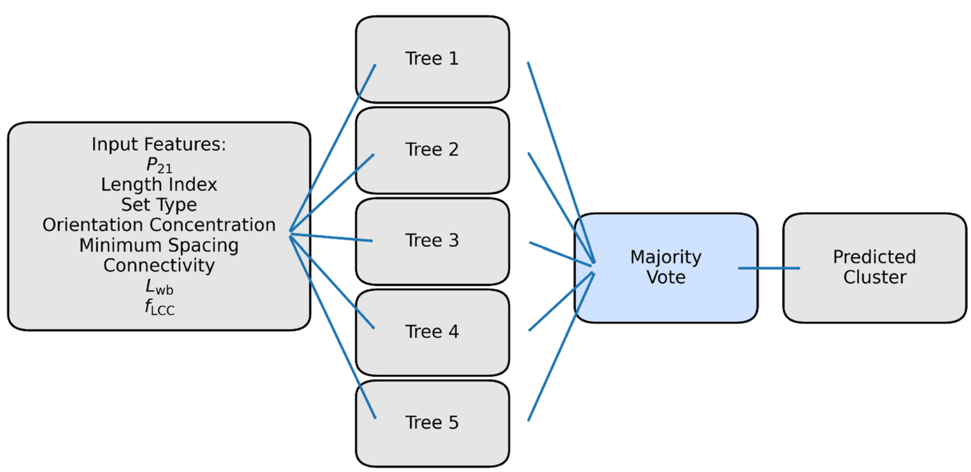

Fig. 3 Structure of the random forest classifier trained to map fracture network properties to the identified flow behaviour classes

2.7 Comparing flow behaviour clusters and GeoTypes across datasets

Dataset comparison is performed to isolate the influence of matrix and fracture permeability configuration on the identified flow behaviour clusters and their associated GeoTypes. Because Datasets A to C share the same DFN ensemble and differ only in the assigned k_m, k_f, and k_f/k_m (Table 2), any change in the optimal number of clusters, cluster membership of individual DFNs, or the associated GeoTypes can be attributed to the permeability configuration rather than to differences in DFN geometry. The comparison therefore evaluates both the consistency of the flow behaviour clusters across different matrix-fracture permeability configurations and the extent to which the resulting GeoTypes remain transferable. For cross-dataset comparison, clusters in Datasets B and C are aligned and relabelled based on maximum overlap in simulation IDs with Dataset A, yielding consistent cluster labels (Clusters 1–n) across datasets.

Cluster consistency across datasets is quantified using pairwise and three-way agreement metrics. Pairwise agreement is defined as the percentage of DFNs that retain the same cluster membership between two datasets, and three-way agreement as the percentage of DFNs that retain the same label across Datasets A, B, and C. Transitions between aligned clusters are additionally visualised using a Sankey diagram [e.g. 85, 86], which summarises the redistribution of DFNs between clusters. In the Sankey diagram, node width is proportional to cluster size and link thickness is proportional to the number of DFNs shared by the connected clusters, such that diagonal links directly indicate cross-cluster transitions, i.e., DFNs that change cluster membership between datasets.

The ranges of fracture network properties associated with each cluster are compared across Datasets A to C. This analysis examines whether a given flow behaviour cluster corresponds to comparable fracture network characteristics under different matrix-fracture permeability configurations, and supports interpretation of why some DFNs retain their cluster membership while others transition between clusters. Feature importance scores derived from random forest classifiers trained independently for each dataset (Fig. 3) are also compared across datasets to assess whether the relative contribution of the key properties to cluster separation shifts when k_m, k_f, and k_f/k_m are modified, and whether such shifts are consistent with the cross-cluster transitions observed in the Sankey diagram.

To evaluate the transferability of GeoTypes across different matrix and fracture permeabilities, medoids from Datasets A to C are compared for each cluster. This comparison assesses whether the clusters in different datasets represent the same pressure derivative behaviour and sequence of flow regimes, such that the same GeoType catalogue can be used regardless of the specific values of k_m and k_f, or whether GeoTypes must be interpreted within the permeability configuration in which they are derived. To enable a consistent comparison between datasets with different matrix and fracture permeabilities, pressure and time variables are transformed into dimensionless form. This ensures that variations in the response reflect fundamental changes in flow behaviour rather than absolute property scaling. Dimensionless time (t_D) and pressure (p_D) are defined as

$$t_D = \frac{k_m t}{\mu \phi_m C_r r_w^2}, \tag{6}$$

$$p_D = \frac{(P_i - P) 2\pi k_m h}{q\mu}, \tag{7}$$

where t is time (s), P_i is initial reservoir pressure (Pa), h is reservoir thickness (m), q is production rate (m^3 s^{-1}), and r_w is wellbore radius (m). The first logarithmic derivative of dimensionless pressure (p'_D) is then computed as

$$p'_D = \frac{dp_D}{d \ln t_D}. \tag{8}$$

 https://doi.org/10.1007/s10596-026-10459-w

3 Results and discussion

The results are first presented for Dataset A, for which the complete workflow is reported in detail. The same procedure is applied independently to Datasets B and C; however, the intermediate steps are not detailed again, as the procedure is identical. The results are then compared across Datasets A to C to evaluate how changes in k_m, k_f, and k_f/k_m affect clustering consistency, the fracture network property ranges associated with each flow behaviour cluster, and the resulting GeoTypes.

3.1 Identification of flow behaviour clusters

Figure 4 shows that for Dataset A, solutions with more than six clusters lead to over-partitioning of the DTW distance space, reflected by a systematic decrease in silhouette score and a corresponding increase in the percentage of misclassified points. Based on the local maxima in silhouette score and the corresponding local minima in percentage of misclassified points, three candidate solutions, $k = 4$, 5, and 6, are selected for further evaluation.

Figure 5 shows that the four-cluster solution forms well-separated groups in the MDS space with clearly distinguishable pressure distributions across clusters. Although the five-cluster solution yields the best statistical clustering quality in Fig. 4, the Davies–Bouldin index and the Calinski–Harabasz index both confirm that the four-cluster solution provides the most compact and well-separated partition of the pressure transient response space, with Davies–Bouldin values of 1.58, 5.21, and 1.97 and Calinski–Harabasz values of 6653, 5079, and 4354 for $k = 4$, 5, and 6, respectively. The sharp deterioration of the Davies–Bouldin index for the five-cluster solution indicates that splitting into five groups introduces at least one pair of clusters that are poorly separated relative to their internal scatter, which is also reflected in the increased overlap observed in the MDS projection. The examination of the medoid pressure distributions for the five- and six-cluster solutions also confirms that the additional clusters do not correspond to physically distinct pressure propagation patterns. Instead, their medoids exhibit pressure distributions that closely resemble those already represented in the four-cluster solution, indicating that these additional clusters arise from statistical over-partitioning rather than meaningful differences in flow behaviour. Thus, the four-cluster solution is selected as the most interpretable representation of the pressure transient variability in Dataset A.

Joint analysis of the fracture network property distributions (Fig. 6) and the corresponding pressure transient responses (Fig. 7) shows that DFNs grouped within the same cluster have comparable ranges of fracture network properties, exhibit a consistent pressure transient shape (i.e. a comparable sequence of flow regimes), and display

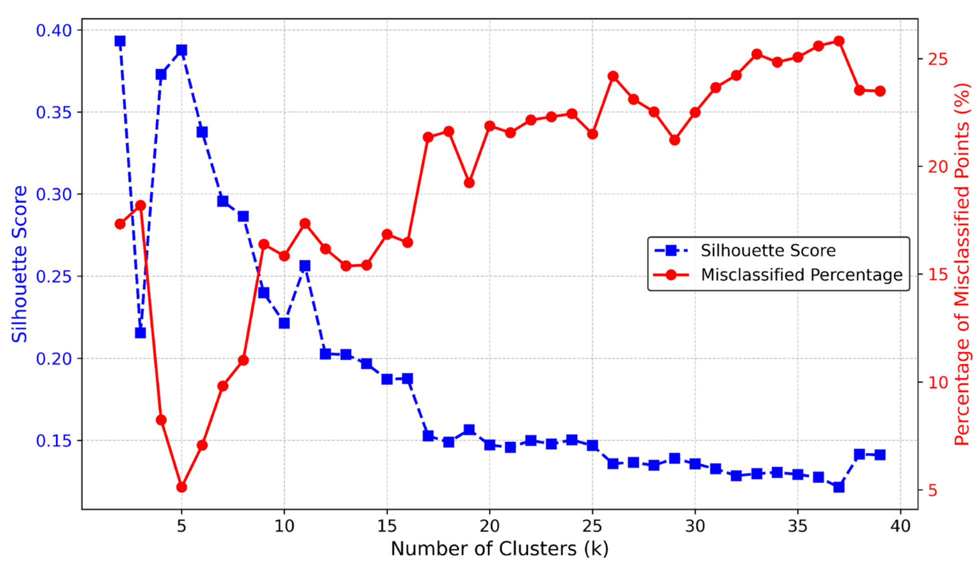

Fig. 4 Average silhouette score and percentage of misclassified points as a function of the number of clusters, k, for the K-medoids clustering applied to the DTW distance matrix for Dataset A

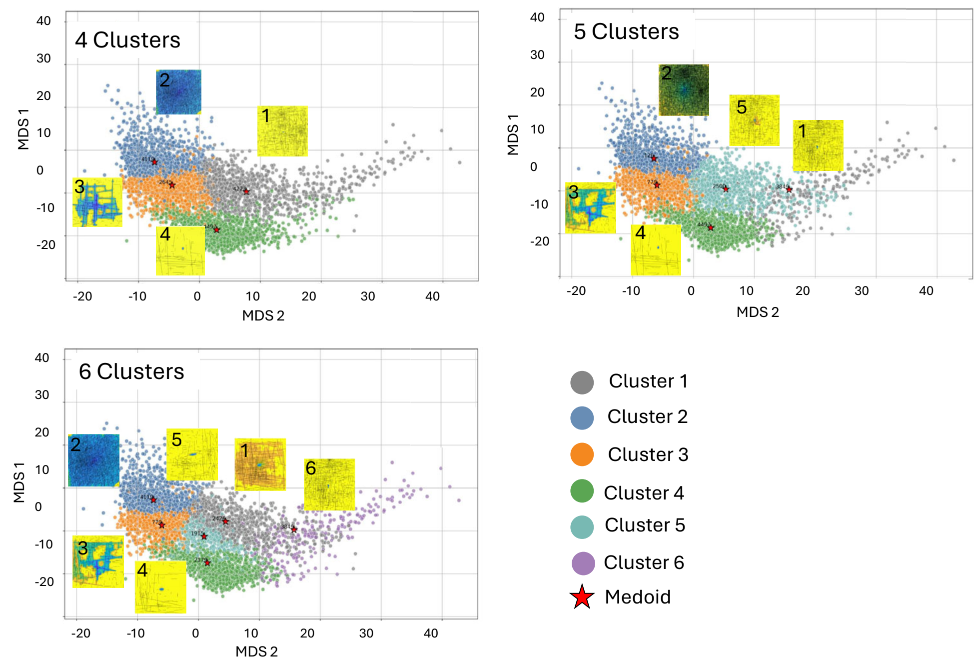

Fig. 5 MDS projection of all pressure response curves in Dataset A. Colours indicate cluster assignments for 4, 5, and 6 cluster solutions. Red stars mark the cluster medoids, and thumbnails show representative pressure distribution of the medoids at the end of the simulation. Results for Dataset B and C are reported in Appendix C (Fig. 16)

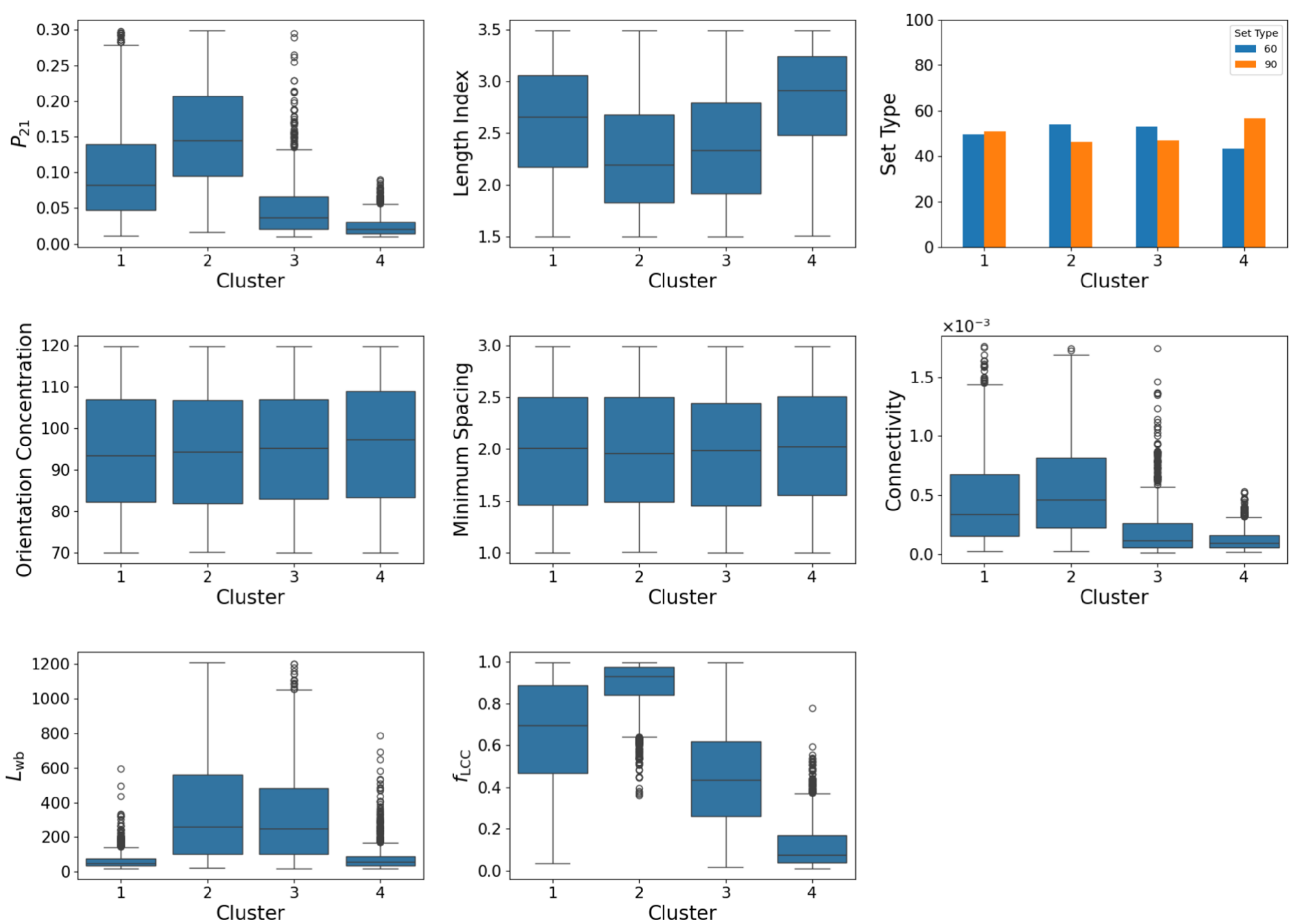

Fig. 6 Box and whisker plots showing the median, P25, and P75 for fracture properties across all clusters, with circles representing the outliers. The fracture set type is a categorised variable representing either orthogonal (90°) or conjugate (60°) fracture sets

 https://doi.org/10.1007/s10596-026-10459-w

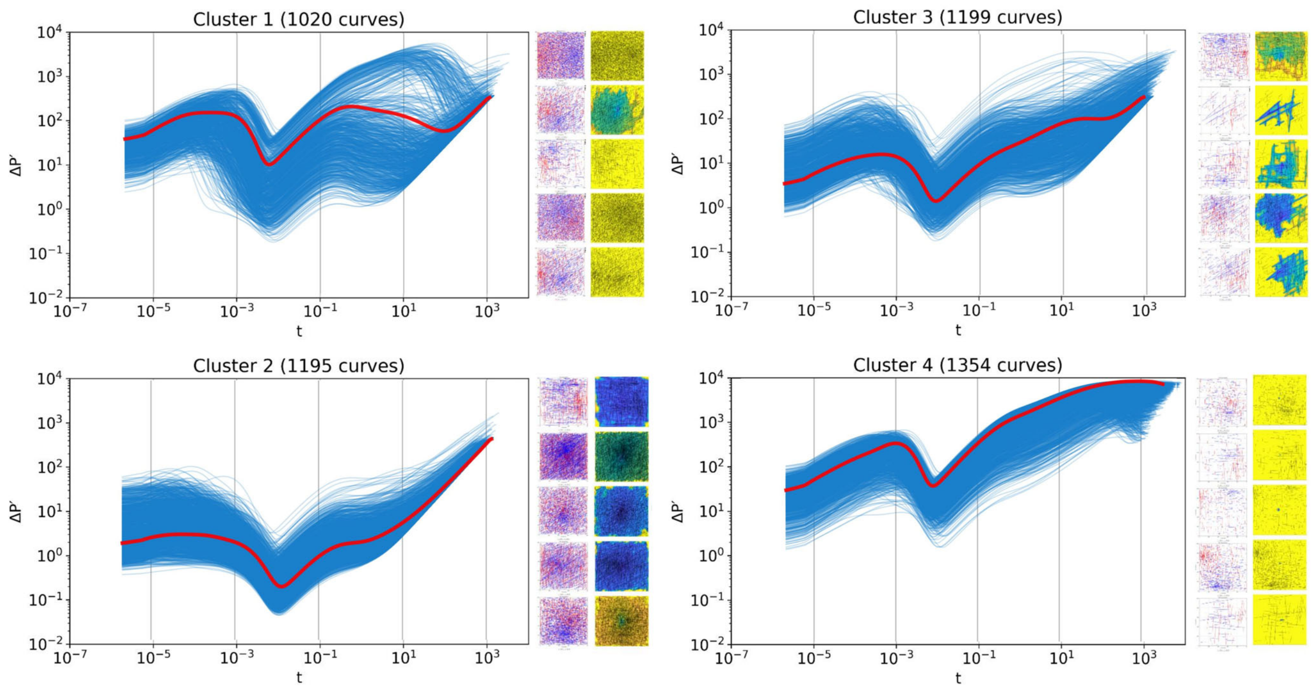

Fig. 7 The log-log diagnostic plot of first derivative of pressure curves for each of the four flow behaviour clusters. Blue lines represent all pressure responses assigned to each cluster, and the red line shows the corresponding cluster medoid. For each cluster, the thumbnails show five randomly selected DFNs (left column) and their associated pressure distributions at the end of the simulation (right column)

similar pressure propagation patterns. In contrast, clusters differ systematically in both the pressure transient responses and the ranges of fracture network properties that characterise them. For example, Cluster 2 is associated with high-intensity and strongly connected fracture networks, with more than 80% of fractures belonging to the backbone, resulting in near-uniform pressure drop across the reservoir domain. Conversely, Cluster 4 corresponds to low-intensity and weakly connected networks, with less than 20% of fractures connected to the backbone, for which pressure drop remains concentrated near the wellbore-intersecting fracture and far-field drainage is limited. Together, these results demonstrate that four clusters provide a geologically meaningful partition of the pressure transient variability in Dataset A.

3.2 Flow regime interpretation of GeoTypes

Using the four flow behaviour clusters, the analysis returns to the cluster medoids to examine the representative pressure transient response of each group. Each medoid summarises the dominant sequence of flow regimes for the DFNs assigned to the cluster and therefore constitutes a pressure transient GeoType described by Corbett et al. [23]. In the following, the GeoTypes are interpreted in terms of their flow regime sequences and corresponding fracture network property ranges, as summarised in Table 3. Flow regime terminology and the associated diagnostic slope behaviour, M, follow the definitions summarised in Appendix B (Table 4).

Cluster 1 is characterised by depletion of a relatively short wellbore-intersecting fracture (median $L_{\mathrm{wb}} = 49.1$ m) embedded within a well-connected fracture backbone (median $f_{\mathrm{LCC}} = 0.694$), with a moderate fracture intensity (median $P_{21} = 0.083$). The pressure transient response initiates with a bilinear flow regime ($M = 0.25$), followed by formation linear flow ($M = 0.5$), reflecting flow within finite-conductivity fractures near the wellbore and subsequent linear migration of fluid from the surrounding matrix toward the fracture [21]. After a brief stabilisation, Cluster 1 shows a double-dip signature consisting of a sharp V-dip followed by a broader U-shaped dip. This sequence reflects two successive storage-exchange processes, depletion of near-well fracture storage and

Table 3 Summary of the identified GeoTypes, their dominant flow-regime sequences, and characteristic fracture property ranges. Values in parentheses represent median values

Cluster	GeoType	Flow-regime sequence	P_{21} (m^{-1})	L_{wb} (m)	f_{LCC}
Cluster 1	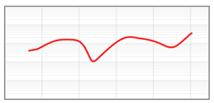	Bilinear ($M = 0.25$) → Linear ($M = 0.5$) → stabilisation ($M \approx 0$) → V-dip → U-dip → boundary dominated ($M = 1$)	0.011–0.298 (0.083)	17.9–597 (49.1)	0.033–0.996 (0.694)
Cluster 2	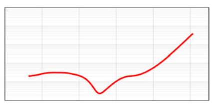	Stabilisation ($M \approx 0$) → negative slope ($M \approx -0.5$) → V-dip → stabilisation ($M \approx 0$) → Linear ($M = 0.5$) → boundary dominated ($M = 1$)	0.0158–0.3 (0.145)	22.2–1.2 × 10^3 (263)	0.36–0.998 (0.93)
Cluster 3	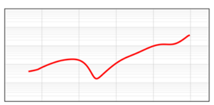	Bilinear ($M = 0.25$) → V-dip → Linear ($M = 0.5$) → stabilisation ($M \approx 0$) → Linear ($M = 0.5$)	0.01–0.295 (0.0374)	20–1.2 × 10^3 (250)	0.0167–0.998 (0.435)
Cluster 4	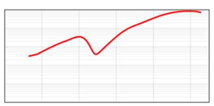	Bilinear ($M = 0.25$) → Linear ($M = 0.5$) → V-dip → Linear ($M = 0.5$) → stabilisation ($M \approx 0$)	0.01–0.0902 (0.0202)	18.7–786 (56.7)	0.0089–0.777 (0.0756)

subsequent engagement of the larger connected backbone structure [87, 88]. At late times, the pressure derivative converges toward a unit-slope trend ($M = 1$), diagnostic of pseudo boundary dominated flow. This behaviour indicates that the pressure transient reaches the finite geometric extent of the connected fracture network, causing fracture storage to be depleted faster than it can be recharged from the matrix [70].

The response of Cluster 2 is governed by a high-intensity (median $P_{21} = 0.145$) and strongly connected fracture network with a dominant backbone (median $f_{\text{LCC}} = 0.93$). Because the well is located in very long fractures (median $L_{\text{wb}} = 263$ m), the pressure derivative rapidly shows a near-horizontal stabilisation flow regime ($M \approx 0$), indicating efficient pressure equilibration within the fracture network. The response then shows a negative slope (approximately -0.5), reflecting a high-diffusivity recharge from highly connected fracture network, which provides a volumetric fluid supply and temporarily offsets the rate of pressure decline. A pronounced V-dip is then observed, indicating matrix-fracture equilibration. Afterwards, the derivative returns to a second stabilisation plateau, where the fluid recharge from the matrix achieves a dynamic balance with the flow discharge of the fracture network [89]. The flow regime then transitions into formation linear flow ($M = 0.5$) for a short time, where fluid is migrating linearly from the matrix toward the connected fracture network and ends with a pseudo boundary dominated flow ($M = 1$).

Cluster 3 exhibits a hybrid response in which a long wellbore-intersecting fracture (median $L_{\text{wb}} = 250$ m) provides access to the connected fracture path, while a lower fracture intensity (median $P_{21} = 0.0374$) and moderate connectivity (median $f_{\text{LCC}} = 0.435$) govern the subsequent behaviour. The early-time response is characterised by a relatively long period of bilinear flow ($M = 0.25$), reflecting extended finite-conductivity flow within the long wellbore-intersecting fracture and along the primary connected pathway. As fluid exchange between the fracture and the surrounding matrix becomes significant, the pressure derivative transitions into a V-dip. This is followed by formation linear flow ($M = 0.5$), reflecting sustained matrix-to-fracture drainage along the accessible fracture path. A short stabilisation period ($M \approx 0$) is then observed, suggesting a temporary balance between fracture depletion and matrix recharge within the limited connected structure. Unlike Clusters 1 and 2, Cluster 3 does not transition into a pseudo boundary dominated flow regime. Instead, the response terminates in a sustained formation linear flow regime ($M = 0.5$). This behaviour reflects depletion of the fractures and continued linear inflow from the surrounding matrix.

Cluster 4 is defined by the lowest fracture intensity (median $P_{21} = 0.0202$) and the lowest f_{LCC} (median $f_{\text{LCC}} = 0.0756$) among all clusters, and relatively short wellbore-intersecting fractures (median $L_{\text{wb}} = 56.7$ m). The early-time behaviour initiates with bilinear flow ($M = 0.25$), reflecting finite-conductivity flow within the wellbore-intersecting fracture, and is followed by formation linear flow ($M = 0.5$). Following depletion of the fracture storage, the V-dip is observed. The derivative returns to a second formation linear flow ($M = 0.5$), which indicates that the sparse, localised nature of the connected network continues to enforce a linear drainage pattern from the matrix even after the inter-porosity transition is complete. The sequence then terminates in a stabilisation period ($M \approx 0$), indicating pseudo-radial flow in which sustained matrix inflow balances the restricted discharge capacity of the sparse fracture network [88].

The link between the representative GeoTypes and distinct ranges of DFN properties demonstrates that the clustering provides an interpretable mapping between pressure transient curves and natural fracture network characteristics. In field applications, the GeoType medoids can be used as reference pressure derivative type curves. A measured pressure derivative response from well test can be compared against the GeoTypes (Fig. 7) to select the closest match and thereby the corresponding flow behaviour cluster. Because each flow behaviour cluster is associated with a distinct range of fracture network properties (Fig. 6), the selected cluster provides initial quantitative bounds on plausible fracture network properties that are consistent with the field response. This matching therefore provides early constraints when developing more detailed geological models, reduces the non-uniqueness inherent to well-test interpretation in naturally fractured reservoirs, and provides an early, physically grounded starting point for history matching and reservoir model calibration. The workflow also supports early risk assessment of projects in fractured reservoirs during the appraisal stage, by translating well-test data into expectations of subsurface flow behaviour, including the relative roles of fractures and matrix in controlling fluid flow, and is best suited to settings where field data are sparse rather than as a substitute for detailed well-test interpretation when more data are available.

3.3 Key fracture network properties controlling GeoTypes

Figure 6 shows that P_{21}, connectivity, L_{wb}, and f_{LCC} differ systematically between clusters, indicating that these parameters most strongly differentiate the dominant flow regimes represented in each GeoType. The length index shows moderate variability, whereas the minimum spacing, orientation concentration, and set type remain broadly consistent across clusters, suggesting that variations in these characteristics do not contribute meaningfully to shaping the GeoTypes.

A random forest classifier is trained on the full set of fracture network properties (Fig. 3) and predicts the flow behaviour class with an accuracy of 73% and a weighted F1-score of 0.73, indicating that the fracture properties contain meaningful information to distinguish between the identified flow behaviour clusters. The moderate classification accuracy reflects that additional sources of variability remain that are not fully resolved by these descriptors alone. The feature importance values derived from the random forest classifier show that the parameters exhibiting larger variations across clusters in Fig. 6 also correspond to higher importance values (Fig. 8(A)). A feature selection step is then applied to remove properties with negligible influence on the predictive accuracy of the model. The reduced model, which retains only P_{21}, L_{wb}, and f_{LCC}, preserves the predictive performance (Fig. 8(B)), indicating that these three fracture network properties capture the primary controls on the pressure transient behaviour and therefore the shape of the GeoType. SHAP analysis of the reduced model quantifies the contribution of P_{21}, L_{wb}, and f_{LCC} to individual class prediction (Fig. 9). L_{wb} and f_{LCC} provide the strongest local contributions to the predictions for Classes 1 and 4, respectively, while P_{21} contributes consistently across all classes. The agreement between the global feature importance and the SHAP-based local contributions confirms that the classifier depends on these same properties when assigning flow behaviour clusters.

The strong influence of L_{wb}, f_{LCC}, and P_{21} on the GeoTypes reflects their direct control on the connectivity and flow behaviour of the fracture network. L_{wb} strongly influences the degree of near-wellbore connectivity and therefore dominates the early-time response, as longer fractures are more likely to intersect additional fractures and

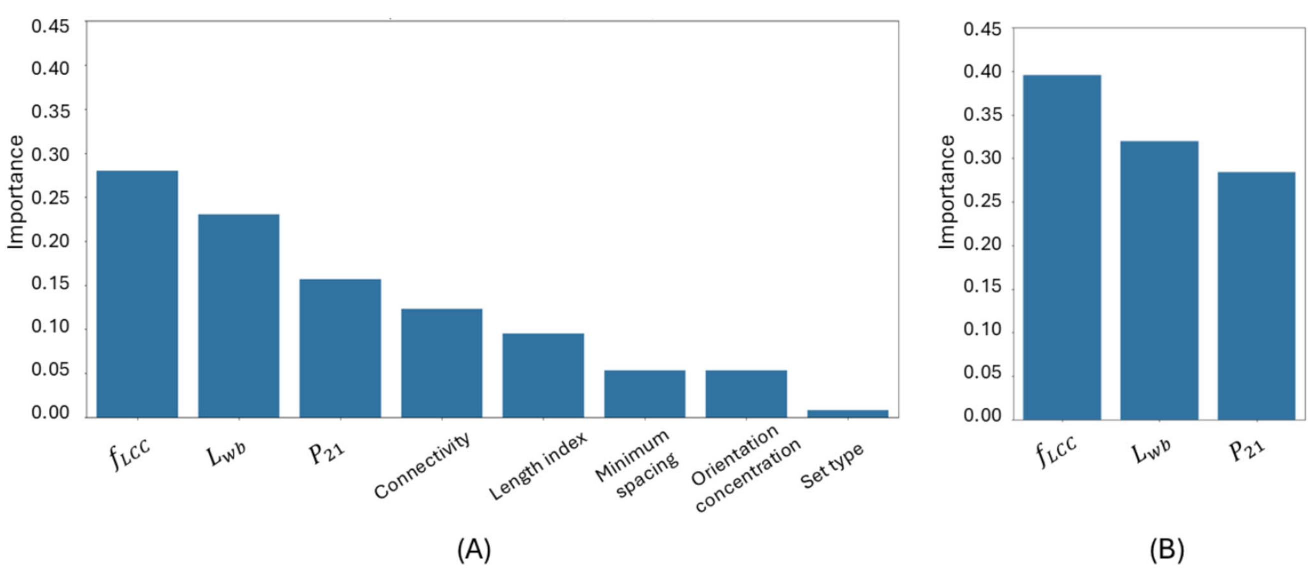

Fig. 8 Feature importance scores derived from the random forest classifier trained on (A) the full set of fracture parameters and (B) the reduced set of fracture parameters

 https://doi.org/10.1007/s10596-026-10459-w

Fig. 9 Mean absolute SHAP values per feature, grouped by cluster. Values indicate the contribution of each parameter to the random-forest classifier's cluster assignment

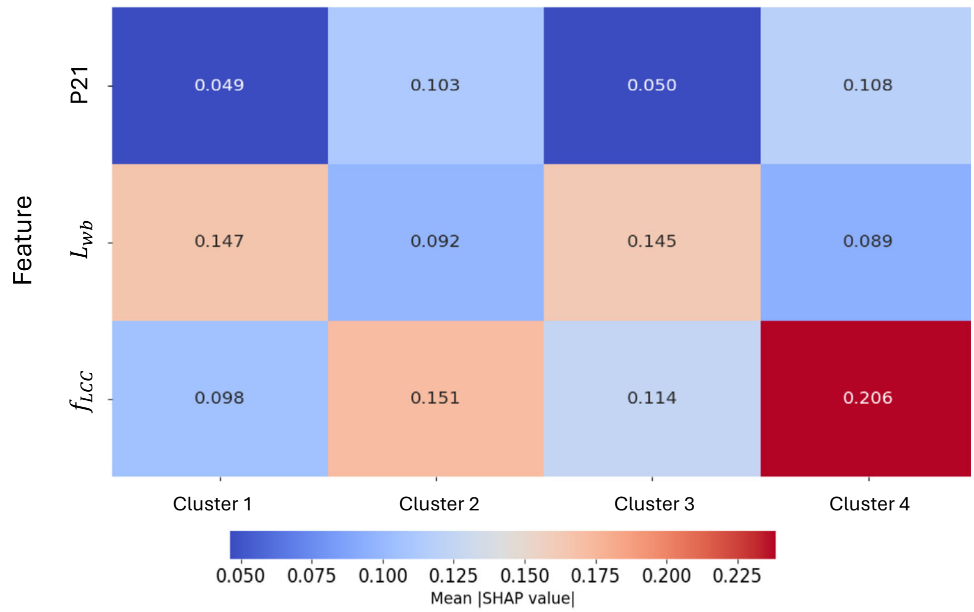

provide high-conductivity flow paths directly connected to the well. The f_{LCC} captures how much of the network participates in forming through-going, preferential flow paths, which can influence the extent of pressure support during the intermediate and late stages of the well test. The prominence of P_{21} highlights the role of overall fracture intensity in defining the magnitude of fracture-dominated flow and the transition between fracture- and matrix-supported flow regimes. Together, these parameters represent the components that most strongly influence how fluid flows in the fracture network, explaining their consistent importance across the clustering and classification results.

3.4 Cross-dataset comparison of flow behaviour clusters and GeoTypes

Applying the full clustering workflow to the pressure transient responses of datasets B and C (Table 2) also resulted in four flow behaviour clusters, consistent with the optimum number of clusters obtained for dataset A (see Appendix C). This agreement suggests that the number of distinct fluid flow behaviours associated with this ensemble of DFNs (and therefore the number of GeoTypes) is primarily governed by the fracture network geometry and remains unchanged when the matrix and fracture permeabilities are scaled uniformly across the network.

However, changes in k_m, k_f, and k_f/k_m can lead to cross-cluster transitions for a subset of DFNs. Pairwise agreement between datasets shows the strongest correspondence in cluster assignment between Datasets B and C (81.5%). The higher agreement is consistent with the shared k_f/k_m contrast in Datasets B and C, which helps preserve the organisation of the clusters, in terms of which DFNs are grouped together. The agreements between Datasets A and C (73.3%) and between Datasets A and B (71.3%) are lower, indicating that independently modifying k_m and k_f, and thereby changing the k_f/k_m contrast, more strongly affects the organisation of the flow behaviour clusters and increases the fraction of DFNs undergoing cross-cluster transitions. When all three datasets are compared simultaneously, 64.1% of DFNs retain the same cluster assignment across all datasets, 33.9% differ in only one dataset, and only 2% receive three entirely different assignments, suggesting that for a majority of networks, the underlying DFN geometry is the dominant control on cluster membership.

The Sankey diagram (Fig. 10) further confirms that cluster membership is largely preserved for individual DFNs across Datasets A, B, and C, as indicated by the dominance of thick links connecting corresponding clusters. Thinner diagonal links connecting different clusters indicate cross-cluster transitions, which occur for a small

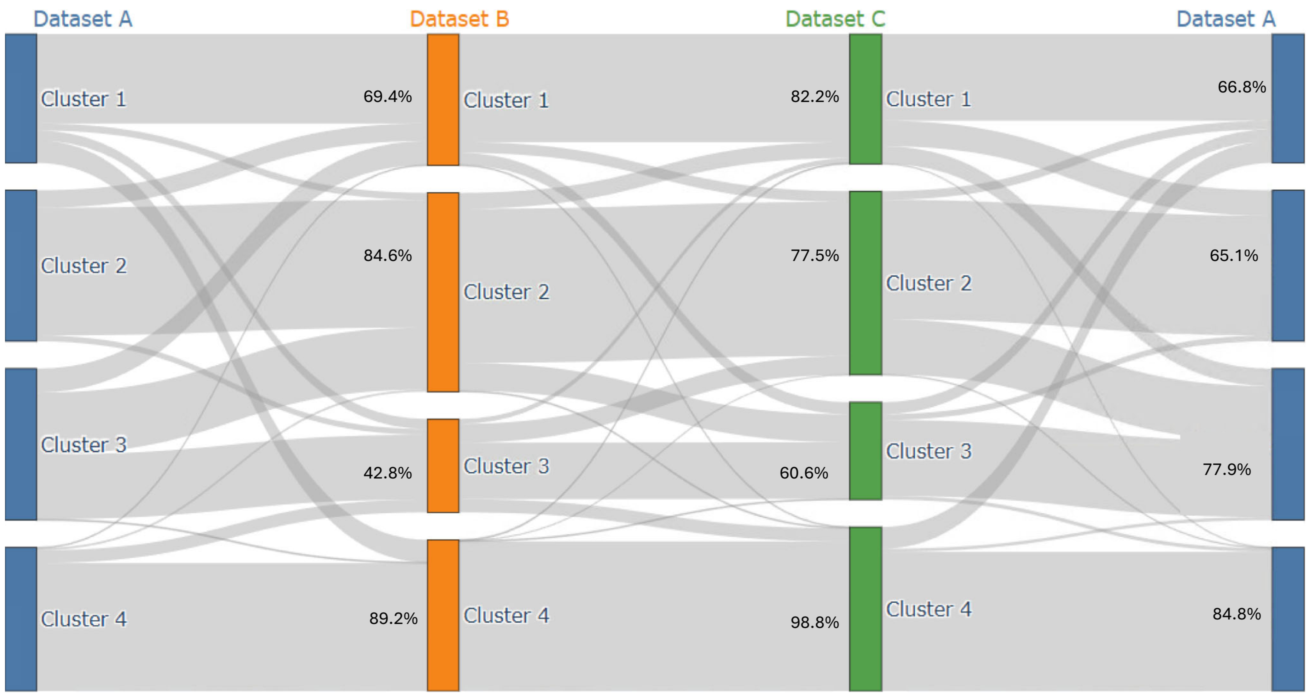

Fig. 10 Sankey diagram illustrating how DFNs transition between the aligned flow behaviour clusters in datasets A, B, and C. Percentages indicate the fraction of DFNs that retain their cluster assignment across datasets

fraction of DFNs when the permeability configuration is modified. This stability is most evident for Cluster 4, which preserves the highest proportion of shared DFNs across all dataset pairs.

Figure 11 shows that the same three key fracture network properties identified in Dataset A, i.e. L_{wb}, f_{LCC}, and P_{21}, also separate the flow behaviour clusters in Datasets B and C. For each cluster, the fracture properties show comparable ranges and medians across datasets, with modest shifts in their absolute values. Clusters 1 to 3 are characterised by higher P_{21} and f_{LCC}, for which pressure diffusion involves coupled fracture–matrix flow and is therefore more sensitive to changes in k_f, k_m, and k_f/k_m. As a result, cross-cluster transitions occur more frequently for these clusters (Fig. 10). Specifically, in Dataset A, where k_f/k_m is lowest, matrix contributions remain significant, and only highly connected and intense fracture networks (high f_{LCC} and P_{21}) exhibit a fully fracture-dominated response (Cluster 2). Networks with moderate connectivity and intensity are therefore grouped into Cluster 3. As k_f/k_m increases in Datasets B and C, flow becomes predominantly fracture-dominated, and networks with moderate f_{LCC} and P_{21} are sufficient to exhibit a fracture-dominated response, transitioning from Cluster 3 to Cluster 2. This transition occurs toward Cluster 2 rather than Cluster 1 because Clusters 2 and 3 share similarly high L_{wb}, while the shift is driven by network-scale properties (f_{LCC} and P_{21}) rather than wellbore-scale characteristics. In contrast, Cluster 4 is consistently defined by the lowest P_{21} and f_{LCC}, such that pressure propagation is dominated by the matrix. Therefore, variations in k_f, k_m, and k_f/k_m have a limited impact on the flow behaviour of the DFNs in Cluster 4, explaining its high consistency across all datasets.

Feature importance derived from the random forest classifier (Fig. 12) further clarifies cross-cluster transitions, showing that the relative importance of the key properties that differentiate the clusters varies between Datasets A, B, and C. For Datasets A and C, f_{LCC} has the highest importance, followed by L_{wb} and P_{21}, whereas in Dataset B, L_{wb} is the most influential parameter, followed by f_{LCC} and P_{21}. This shift in feature importance implies that the relative role of fracture network properties in controlling cluster separation depends on matrix-fracture permeability configurations. As a result, DFNs with intermediate combinations of f_{LCC}, L_{wb}, and P_{21} (Clusters 1 and 3), are more sensitive to changes in k_f, k_m, and k_f/k_m because small shifts in the relative contribution of fractures and matrix can move their pressure derivative response into closer agreement with a different GeoType, consistent with the cross-cluster transitions in Fig. 10.

 https://doi.org/10.1007/s10596-026-10459-w

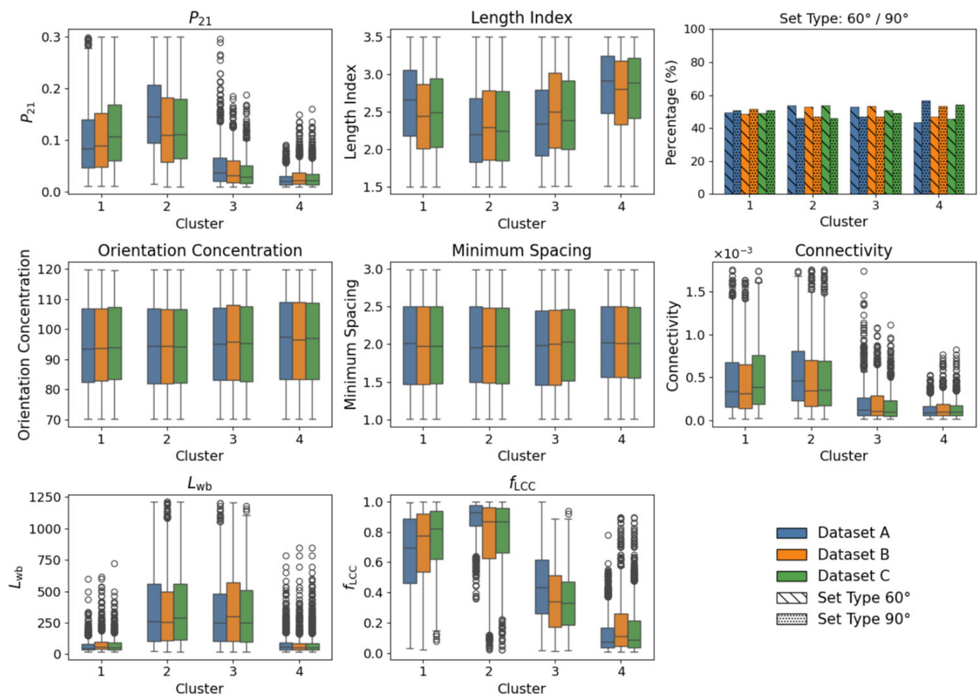

Fig. 11 Box and whisker plots showing the median, P25, and P75 for fracture properties across four clusters for Dataset A, B, and C, with circles representing the outliers. The fracture set type is a categorised variable representing either orthogonal (90°) or conjugate (60°) fracture sets

Comparing the GeoTypes across datasets reveals that they change systematically when matrix and fracture permeabilities are changed (Fig. 13). For each cluster, GeoTypes of different datasets exhibit differences in early-time derivative magnitude, the presence and prominence of the V-dip, and the overall sequence and duration of flow regimes. Because each Cluster 1 to 4 corresponds to comparable ranges of DFN properties across all datasets (Fig. 11), these shifts indicate that while DFN geometry largely determines which DFNs are clustered together, the absolute values of k_m, k_f, and the k_f/k_m contrast govern the specific flow behaviour associated with that cluster.

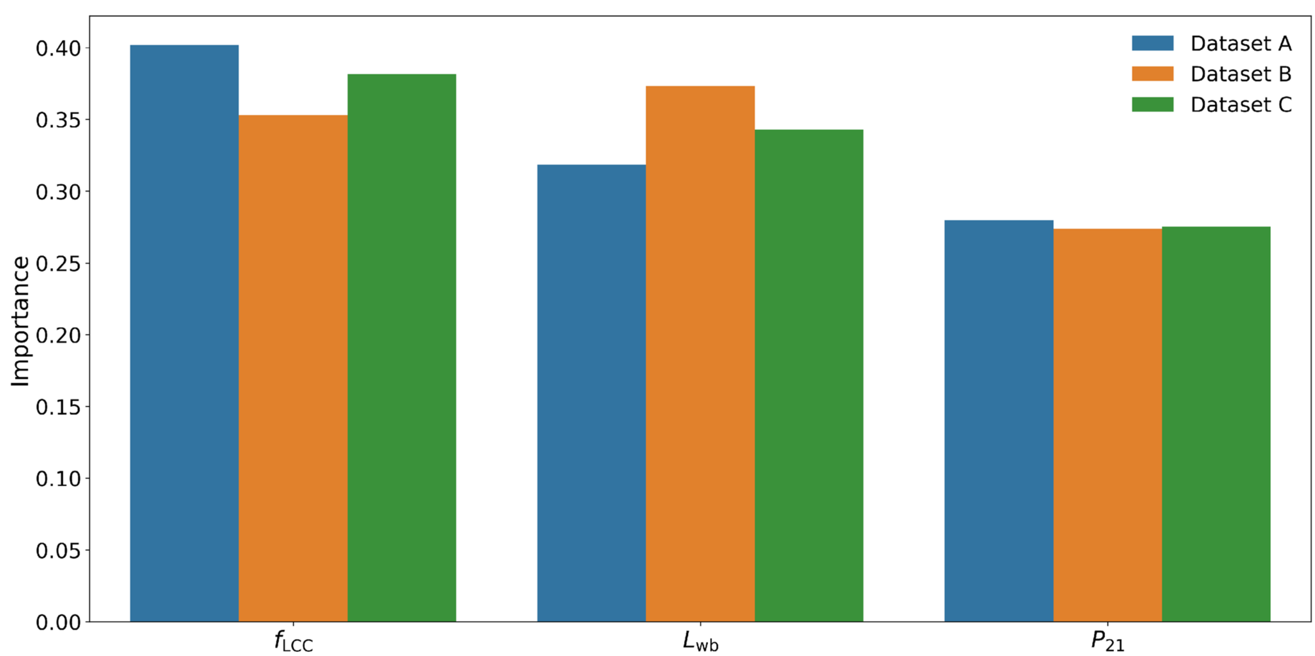

Fig. 12 Feature importance scores from random forest classifiers trained independently on Datasets A, B, and C using a reduced set of fracture network properties, f_{LCC}, L_{wb}, and P_{21}, as inputs and the cluster labels as outputs

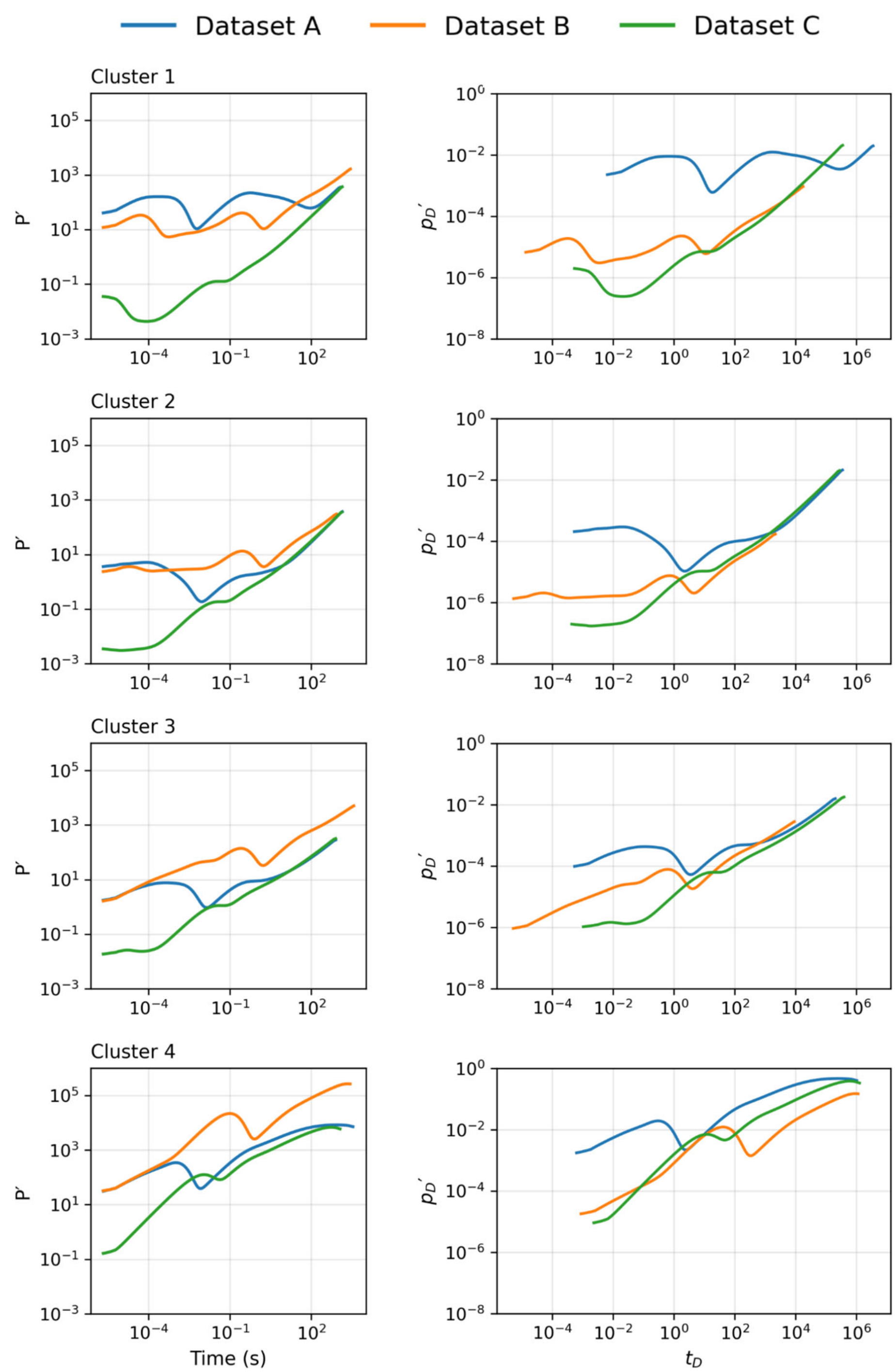

Fig. 13 Comparison of GeoTypes across Datasets A, B, and C. Rows correspond to Clusters 1 to 4. Left panels show the first pressure derivative, P', and right panels show the corresponding dimensionless derivative, p'_D. Colours denote datasets (A: blue, B: orange, C: green)

To examine how the pressure transient response changes across datasets for a fixed DFN geometry, we compare the responses of three DFNs per cluster that retain their cluster label across Datasets A, B, and C (Fig. 14). This comparison isolates the impact of the permeability configuration from that of the DFN geometry, allowing us to investigate how a same fracture network architecture generates different GeoTypes under different matrix-fracture permeability configurations.

Two observations are consistent across all clusters. First, the V-dip is always the least pronounced in Dataset C. In contrast, the depth and shape of the V-dip are comparable for Datasets A and B. Following Eq. 1, this difference is explained by variations in the fracture storage term, $\phi_f C_{t,f}$, and its effect on the storativity ratio,

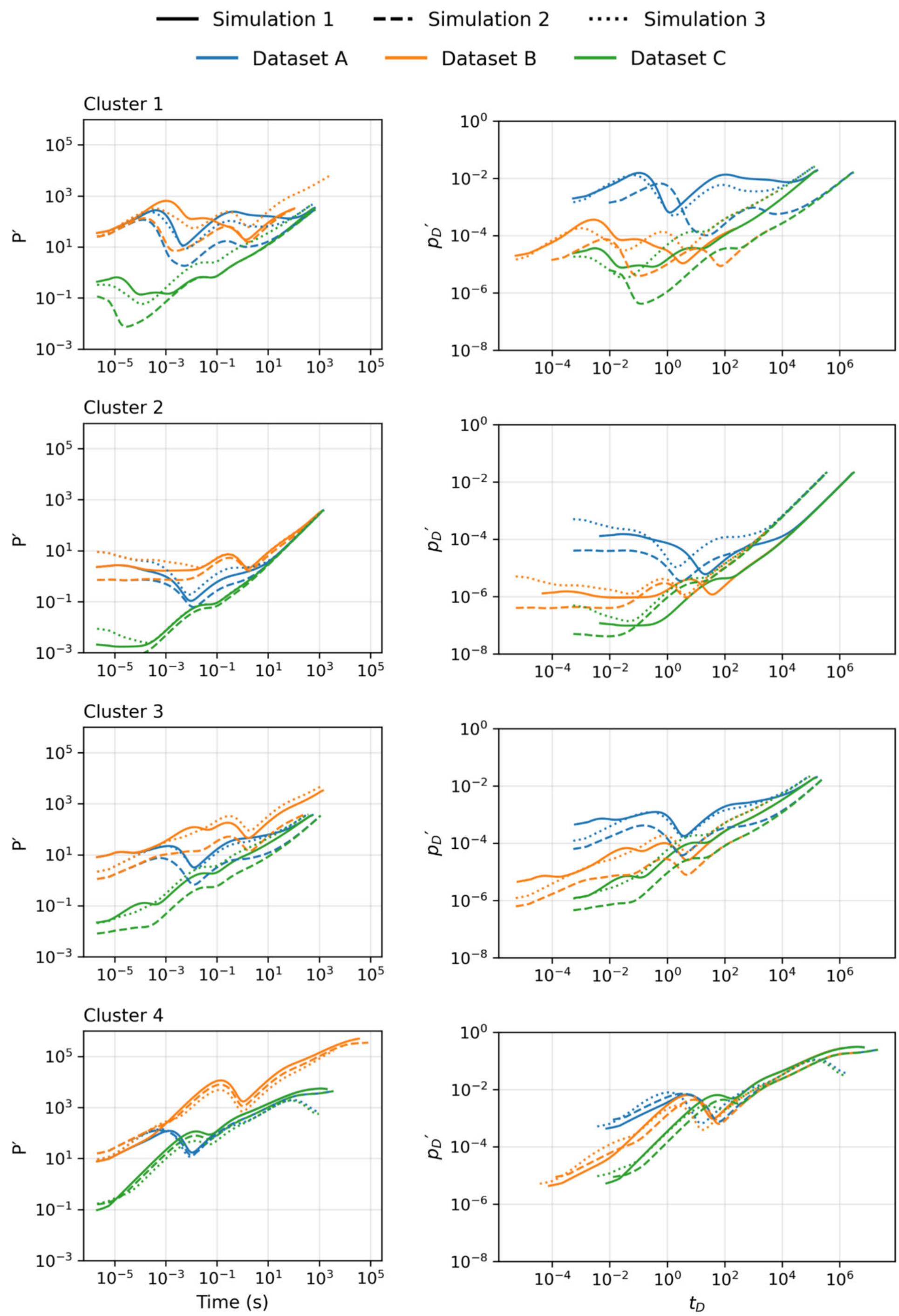

Fig. 14 Comparison of pressure transient responses across Datasets A, B, and C for the flow behaviour clusters. Rows correspond to Clusters 1 to 4. Left panels show the first pressure derivative, P', and right panels show the corresponding dimensionless derivative, p'_D. Colours denote datasets (A: blue, B: orange, C: green), and line styles represent three randomly selected shared simulations (Simulation 1–3)

ω. Datasets A and B have the same fracture aperture range (5×10^{-4} to 4×10^{-3} m), implying comparable fracture porosity ϕ_f and therefore similar ω, which is consistent with the similarly in the shape and depth of their V-dip. A more pronounced V-dip indicates more limited fracture storage relative to the matrix and a longer delay before matrix recharge stabilises the fracture pressure. In contrast, the apertures in Dataset C are an order of magnitude larger (5×10^{-3} to 4×10^{-2} m), which increases ϕ_f and ω and attenuates the V-dip; a less pronounced V-dip therefore indicates greater fracture storage and faster fracture–matrix equilibration. In several simulations for Dataset C (particularly in Clusters 2 and 3), the V-dip is replaced by a stabilisation period ($M \approx 0$), indicating near-instantaneous fracture–matrix pressure equilibration. Although Datasets B and C share the same k_f/k_m

contrast, Dataset C has k_f and k_m values that are 100 times higher. This high absolute conductivity reduces the timescale of fracture–matrix pressure equilibration, such that the matrix recharge stabilises the pressure drop in the fracture network almost instantaneously. Thus the reservoir behaves similar to a homogeneous medium and the V-dip is not observed.

A second observation consistent across all clusters is that, for a fixed DFN geometry, the early-time p'_D magnitude follows a systematic ordering: the initial derivative value is primarily controlled by the effective fracture transmissivity and the fracture–matrix permeability contrast, with Dataset A exhibiting the highest values, followed by Dataset B, and Dataset C showing the lowest. This behaviour reflects differences in the near-wellbore flow capacity imposed by the fracture permeability and its contrast with the matrix. Dataset C contains the highest fracture permeabilities, which provide the largest early-time transmissivity around the well and therefore the lowest p'_D magnitudes (Table 2). Datasets A and B share a lower fracture permeability range, resulting in higher derivatives overall. Between these two, Dataset B yields slightly lower p'_D than Dataset A because its very low matrix permeability ($k_m = 10^{-16}\,\mathrm{m}^2$) makes the early response almost purely fracture-dominated, whereas in Dataset A the higher matrix permeability ($k_m = 10^{-14}\,\mathrm{m}^2$) and lower k_f/k_m contrast reduce the effective dominance of the fractures and thus produce the highest early-time derivative.

These differences demonstrate that pressure transient GeoTypes are not universal type curves defined solely by the geometry of the DFN; instead, they are jointly dependent on the permeability configuration. While the underlying geometry (L_{wb}, f_{LCC}, and P_{21}) determines the broad cluster assignment, the absolute values of k_m, k_f, and k_f/k_m can shape the visibility and timing of flow regime transitions. Consequently, a single set of GeoTypes cannot be treated as a static template across all reservoirs; rather, GeoTypes must be interpreted within the specific fracture and matrix permeability configuration in which they are derived. The practical value of the GeoType framework is therefore not to provide a single curve to fit, but to narrow the plausible parameter space and guide data acquisition and calibration towards the fracture network properties that matter most for fluid flow in the system.

4 Conclusion

This study establishes an unsupervised machine learning workflow to characterise fractured reservoirs by linking pressure transient responses to fracture network properties. The approach clusters pressure-derivative responses using K-medoids with DTW as a similarity metric to define GeoTypes for a geologically consistent ensemble of DFNs.

Across all three datasets, the workflow identifies four distinct clusters, suggesting that the number of flow behaviour groups in this DFN ensemble is primarily governed by the fracture network geometry. For each dataset, each cluster is characterised by a distinct and repeatable sequence of diagnostic flow regimes that are physically consistent with a constrained range of fracture network properties. The cluster medoids therefore provide GeoTypes that constrain uncertainty in field well-test interpretation by linking a measured pressure derivative response to bounded ranges of plausible fracture network properties. Using random forest classification supported by SHAP values identifies P_{21}, L_{wb}, and f_{LCC} as the key fracture network properties in shaping distinct fluid flow behaviour. Consequently, improved characterisation of fractured reservoirs benefits from sampling these properties at higher resolution and constraining them more tightly.

Comparison across datasets shows that most DFNs retain their flow behaviour cluster, suggesting that cluster membership is primarily controlled by fracture network geometry. Cluster transitions occur mainly for moderately connected DFNs, which are sensitive to the balance of coupled fracture-matrix interactions and can shift between flow behaviour clusters when the fracture and matrix permeability configuration is modified. Analysis of transient responses for fixed DFN geometries across the three datasets reveals systematic changes in their pressure derivative behaviour. These changes demonstrate that while the fracture geometry defines the broad flow behaviour classification, the absolute values of k_m, k_f, and k_f/k_m shape the visibility, timing, and prominence of specific flow regimes and their transitions. GeoTypes are therefore not identical across datasets and cannot be considered as universal type curves, but must be interpreted within the matrix-fracture permeability context in which they are derived.

Overall, the proposed framework provides a methodology to constrain geological uncertainty and enhance the reliability of reservoir characterisation in complex fractured systems. By identifying a limited number of repeatable flow behaviour clusters and linking them to bounded ranges of fracture network properties, the workflow reduces the non-uniqueness inherent in conventional well-test interpretation. It also offers practical guidance for data acquisition by highlighting which fracture network properties must be constrained more tightly to support robust prediction of reservoir flow behaviour. The findings are particularly suited to early decision making and de-risking in projects involving fractured reservoirs. For example, in fractured geothermal reservoirs, early identification of the dominant flow behaviour provides immediate constraints on the relative contributions of fractures and matrix to fluid flow, and supports early identification of through-going, highly connected fracture architectures that are prone to rapid thermal breakthrough and reduced thermal performance. Validating these capabilities against field well-test data, where wellbore storage, skin effects, and observational noise are present, represents an important direction for future work.

Supplementary information

The datasets and source code used in this study are publicly available through 4TU.ResearchData at https://doi.org/10.4121/8291d285-025d-4724-988d-fc747a578c0a. The repository includes the generated DFN ensembles, pressure transient simulation outputs, and the machine-learning workflows required to reproduce the results presented in this paper. The open source GeoDFN software is available at https://doi.org/10.4121/0dc9c47a-2294-4811-a0fe-e049cb15ff3d and MRST at https://www.sintef.no/projectweb/mrst/.

Appendix A: LHS sample size selection

To determine an appropriate LHS sample size, we monitored the stabilisation of the mean and variance of the fracture network properties varied in the DoE (Table 1) as the number of sampled parameter combinations was

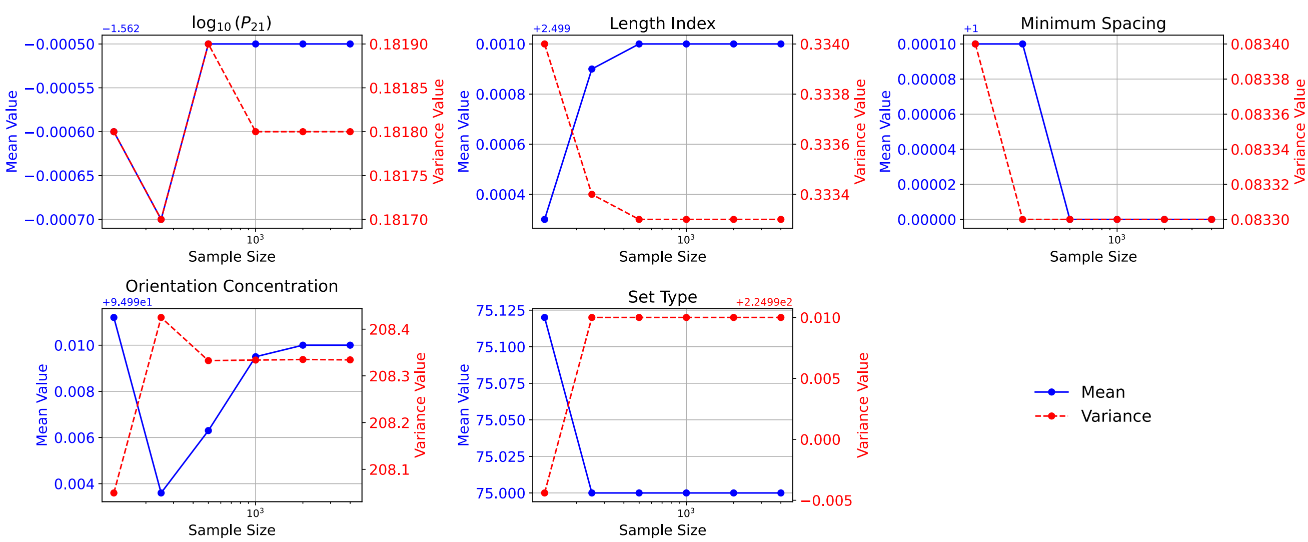

Fig. 15 Mean (blue line, left axis) and variance (red dashed line, right axis) of selected fracture network properties as a function of LHS sample size

increased. Figure 15 shows that these statistics stabilise at approximately 1000 samples, which we therefore adopt for the DoE.

Appendix B: Catalogue of flow regimes and diagnostic features

Table 4 summarises the flow regimes and associated diagnostic behaviour observed in this study. Flow regimes are identified from characteristic slopes on the log–log pressure derivative plot. The local slope M is defined as

$$M = \frac{d\log(P')}{d\log(t)}. \tag{B1}$$

Table 4 Catalogue of flow regimes and diagnostic features used in this study

Flow regime	M	Fluid flow behaviour
Bilinear flow	0.25	Finite-conductivity fracture flow coupled with linear flow in the surrounding formation [21].
Formation linear flow	0.5	One-dimensional flow, typically reflecting matrix-to-fracture drainage or flow along a dominant fracture pathway [21].
Pseudo-radial flow	0	Near-horizontal derivative behaviour indicating pressure equilibration within the fracture network or a dynamic balance between matrix inflow and fracture-network discharge [88, 89].
Pseudo boundary dominated flow	1.0	Late-time unit-slope behaviour indicating that the pressure transient has reached the finite extent of the connected fracture network [70].

Appendix C: Number of clusters and MDS visualisation for datasets B and C

Figure 16 shows the MDS projections of the pressure transient responses for Datasets B and C, where four distinct clusters are evident, consistent with the clustering structure identified in Dataset A. For the four-cluster solution, the clustering performance metrics remain comparable across datasets. In Dataset B, the silhouette score, Davies–Bouldin index, and Calinski–Harabasz index are 0.3736, 1.0445, and 5367.4941, respectively. In Dataset C, these values are 0.4551, 0.9615, and 5399.7173. These results indicate that the clustering remains well-defined across different k_f/k_m configurations.

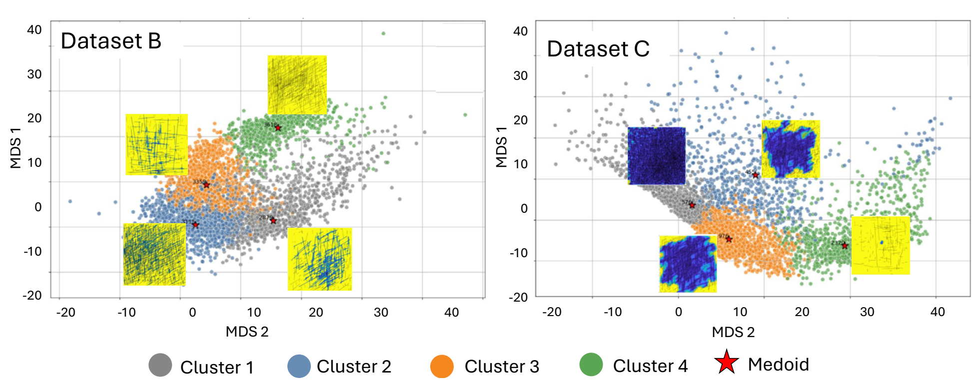

Fig. 16 MDS projections of all pressure response curves for Datasets B and C, showing the four-cluster structure, with data points coloured by cluster assignment. Red stars indicate cluster medoids, and thumbnails show the representative pressure distributions of the medoids at the end of the simulation

Acknowledgements The authors thank Energi Simulation for funding this research. We also thank the anonymous reviewers for their constructive feedback and insightful comments that helped us to improve the original manuscript.

Author Contributions E.K. implemented the codes, conducted the analysis, and wrote the manuscript. G.R., P.-O.B., A.D., and S.G. supervised the work, contributed to the conceptualisation of the study and the development of the methodology, and provided critical revisions. All authors reviewed the manuscript and approved the final version.

Data Availability The datasets and source code used in this study are publicly available through 4TU.ResearchData at https://doi.org/10.4121/8291d285-025d-4724-988d-fc747a578c0a. The repository includes the generated DFN ensembles, pressure transient simulation outputs, and the machine-learning workflows required to reproduce the results presented in this paper. The open source GeoDFN software is available at https://doi.org/10.4121/0dc9c47a-2294-4811-a0fe-e049cb15ff3d and MRST at https://www.sintef.no/projectweb/mrst/.

Declarations

Competing interests The authors declare no competing interests.

References

1. Viswanathan, H.S., Ajo-Franklin, J., Birkholzer, J.T., Carey, J.W., Guglielmi, Y., Hyman, J.D., Karra, S., Pyrak-Nolte, L.J., Rajaram, H., Srinivasan, G., Tartakovsky, D.M.: From Fluid Flow to Coupled Processes in Fractured Rock: Recent Advances and New Frontiers. Rev. Geophys. **60**(1), 2021–000744 (2022). https://doi.org/10.1029/2021RG000744
2. Berkowitz, B.: Characterizing flow and transport in fractured geological media: A review. Adv. Water Resour. **25**(8–12), 861–884 (2002). https://doi.org/10.1016/S0309-1708(02)00042-8
3. Vidal, J., Genter, A., Chopin, F.: Permeable fracture zones in the hard rocks of the geothermal reservoir at Rittershoffen, France. Journal of Geophysical Research: Solid Earth. **122**(7), 4864–4887 (2017). https://doi.org/10.1002/2017JB014331
4. Medici, G., Smeraglia, L., Torabi, A., Botter, C.: Review of Modeling Approaches to Groundwater Flow in Deformed Carbonate Aquifers. Groundwater **59**(3), 334–351 (2021). https://doi.org/10.1111/GWAT.13069
5. March, R., Doster, F., Geiger, S.: Assessment of CO2 Storage Potential in Naturally Fractured Reservoirs With Dual-Porosity Models. Water Resour. Res. **54**(3), 1650–1668 (2018). https://doi.org/10.1002/2017WR022159
6. Cao, M., Sharma, M.M.: Effect of fracture geometry, topology and connectivity on energy recovery from enhanced geothermal systems. Energy **282**, 128368 (2023). https://doi.org/10.1016/J.ENERGY.2023.128368
7. Heinze, T., Gunatilake, T.: Estimating the heat transfer in fractured geothermal reservoirs. Energy. **321**, 135008 (2025) 10.1016/J.ENERGY.2025.135008
8. Fadel, M., Reinecker, J., Bruss, D., Moeck, I.: Causes of a premature thermal breakthrough of a hydrothermal project in Germany. Geothermics **105**, 102523 (2022). https://doi.org/10.1016/J.GEOTHERMICS.2022.102523
9. Iding, M., Ringrose, P.: Evaluating the impact of fractures on the performance of the In Salah CO2 storage site. Int. J. Greenhouse Gas Control **4**(2), 242–248 (2010). https://doi.org/10.1016/J.IJGGC.2009.10.016
10. Snippe, J., Kampman, N., Bisdom, K., Tambach, T., March, R., Maier, C., Phillips, T., Inskip, N.F., Doster, F., Busch, A.: Modelling of long-term along-fault flow of CO2 from a natural reservoir. Int. J. Greenhouse Gas Control **118**(3), 103666 (2022). https://doi.org/10.1016/j.ijggc.2022.103666
11. Yao, M., Chang, H., Li, X., Zhang, D.: Tuning Fractures With Dynamic Data. Water Resour. Res. **54**(2), 680–707 (2018). https://doi.org/10.1002/2017WR022019
12. Lepillier, B., Daniilidis, A., Doonechaly Gholizadeh, N., Bruna, P.O., Kummerow, J., Bruhn, D.: A fracture flow permeability and stress dependency simulation applied to multi-reservoirs, multi-production scenarios analysis. Geothermal Energy. **7**(1), 1–16 (2019). https://doi.org/10.1186/S40517-019-0141-8

13. Lepillier, B., Bruna, P.O., Bruhn, D., Bastesen, E., Daniilidis, A., Garcia, O., Torabi, A., Wheeler, W.: From outcrop scanlines to discrete fracture networks, an integrative workflow. J. Struct. Geol. **133**, 103992 (2020). https://doi.org/10.1016/J.JSG.2020.103992
14. Steffens, B.: Integrating geological uncertainty and dynamic data into modelling procedures for fractured reservoirs, Edinburgh (2022). (PhD thesis)
15. Corbett, P.W.M., Geiger, S., Borges, L., Garayev, M., Gonzalez, J.G., Valdez, C.: Limitations in numerical well rest modelling of fractured carbonate rocks. 72nd European association of geoscientists and engineers conference and exhibition 2010: A new spring for geoscience. Incorporating SPE EUROPEC **2010**(2), 1135–1145 (2010). https://doi.org/10.2118/130252-MS
16. Corbett, P.W.M., Geiger, S., Borges, L., Garayev, M.: The third porosity system: understanding the role of hidden pore systems in well-test interpretation in carbonates. Pet. Geosci. **18**(1), 73–81 (2012). https://doi.org/10.1144/1354-079311-010
17. Egya, D.O., Geiger, S., Corbett, P., March, R., Bisdom, K., Bertotti, G., Bezerra, F.: Analysing the limitations of the dual-porosity response during well tests in naturally fractured reservoirs. Pet. Geosci. **25**(1), 30–49 (2019). https://doi.org/10.1144/PETGEO2017-053/CITE/REFWORKS
18. Egya, D.O., Corbett, P.W., Geiger, S., Norgard, J.P., Hegndal-Andersen, S.: Calibration of naturally fractured reservoir models using integrated well-test analysis - an illustration with field data from the Barents Sea. Petroleum Geoscience **28**(1), (2022). https://doi.org/10.1144/PETGEO2020-042
19. Bourdet, D.: Well test analysis: The use of advanced interpretation models, vol. 3, (2002)
20. Gringarten, A.C.: Interpretation of tests in fissured and multilayered reservoirs with double-porosity behavior: Theory and practice. J. Petrol. Technol. **36**(04), 549–564 (1984). https://doi.org/10.2118/10044-PA
21. Kuchuk, F., Onur, M., Hollaender, F.: Pressure transient formation and well testing: Convolution, deconvolution and nonlinear estimation, vol. 57, (2010)
22. Warren, J.E., Root, P.J.: The behavior of naturally fractured reservoirs. Soc. Petrol. Eng. J. **3**(03), 245–255 (1963). https://doi.org/10.2118/426-PA
23. Corbett, P.W.M., Ellabad, Y., Egert, J.I.K., Zheng, S.: The geochoke well test response in a catalogue of systematic geotype curves. In: All Days. SPE, (2005). https://doi.org/10.2118/93992-MS
24. Freites, A., Corbett, P., Rongier, G., Geiger, S.: Automated classification of well test responses in naturally fractured reservoirs using unsupervised machine learning. Transp. Porous Media **147**(3), 747–779 (2023). https://doi.org/10.1007/S11242-023-01929-1/FIGURES/20
25. Kamel Targhi, E., Bruna, P.-O., Daniilidis, A., Rongier, G., Geiger, S.: From outcrop observations to dynamic simulations: An efficient workflow for generating ensembles of geologically plausible fracture networks and assessing their impact on flow and transport. Geoenergy. (2025). https://doi.org/10.1144/GEOENERGY2025-028
26. Lee, S.H., Lough, M.F., Jensen, C.L.: Hierarchical modeling of flow in naturally fractured formations with multiple length scales. Water Resour. Res. **37**(3), 443–455 (2001). https://doi.org/10.1029/2000WR900340
27. Li, L., Lee, S.H.: Efficient field-scale simulation of black oil in a naturally fractured reservoir through discrete fracture networks and homogenized media. SPE Reserv. Eval. Eng. **11**(04), 750–758 (2008). https://doi.org/10.2118/103901-PA
28. Davy, P., Le Goc, R., Darcel, C.: A model of fracture nucleation, growth and arrest, and consequences for fracture density and scaling. J. Geophys. Res.: Solid Earth **118**(4), 1393–1407 (2013). https://doi.org/10.1002/JGRB.50120
29. Welch, M.J., Lüthje, M., Oldfield, S.J.: Modelling the evolution of natural fracture networks: Methods for simulating the nucleation, propagation and interaction of layer-bound fractures. Modelling the Evolution of Natural Fracture Networks: Methods for Simulating the Nucleation, Propagation and Interaction of Layer-Bound Fractures, 1–230 (2020). https://doi.org/10.1007/978-3-030-52414-2/COVER
30. Kamel Targhi, E., Bruna, P.-O., Daniilidis, A., Rongier, G., Geiger, S.: Machine learning for geologically consistent flow analysis in fractured geothermal reservoirs: A case study. **2025**(1), 1–5 (2025). https://doi.org/10.3997/2214-4609.2025101257
31. Bisdom, K., Nick, H.M., Bertotti, G.: An integrated workflow for stress and flow modelling using outcrop-derived discrete fracture networks. Comput. Geosci. **103**, 21–35 (2017). https://doi.org/10.1016/J.CAGEO.2017.02.019
32. Hupkes, J., Bruna, P.O., Bertotti, G., Doesburg, M., Moscariello, A.: A fracture rarely comes alone: associations of fractures and stylolites in analogue outcrops improve borehole image interpretations of fractured carbonate geothermal reservoirs. Solid Earth **17**(1), 113–134 (2026). https://doi.org/10.5194/se-17-113-2026
33. Jafari, A., Babadagli, T.: Estimation of equivalent fracture network permeability using fractal and statistical network properties. J. Petrol. Sci. Eng. **110**(123), 92–93 (2012). https://doi.org/10.1016/J.PETROL.2012.06.007
34. Agbaje, T.Q., Ghanbarian, B., Hyman, J.D.: Effective permeability in fractured reservoirs: Discrete fracture matrix simulations and percolation-based effective-medium approximation. Water Resour. Res. **59**(11), 2023–036505 (2023). https://doi.org/10.1029/2023WR036505
35. Bogdanov, I.I., Mourzenko, V.V., Thovert, J.-F., Adler, P.M.: Effective permeability of fractured porous media with power-law distribution of fracture sizes. Phys. Rev. E (2003). https://doi.org/10.1103/PhysRevE.76.036309
36. Bai, T., Pollard, D.D.: Fracture spacing in layered rocks: A new explanation based on the stress transition. J. Struct. Geol. **22**(1), 43–57 (2000). https://doi.org/10.1016/S0191-8141(99)00137-6

37. Welch, M.J., Luthje, M., Glad, A.C.: Influence of fracture nucleation and propagation rates on fracture geometry: Insights from geomechanical modelling. Pet. Geosci. **25**(4), 470–489 (2019). https://doi.org/10.1144/PETGEO2018-161
38. Bonnet, E., Bour, O., Odling, N.E., Davy, P., Main, I., Cowie, P., Berkowitz, B.: Scaling of fracture systems in geological media. Rev. Geophys. **39**(3), 347–383 (2001). https://doi.org/10.1029/1999RG000074
39. Liu, R., Li, B., Jiang, Y., Huang, N.: Review: Mathematical expressions for estimating equivalent permeability of rock fracture networks. Hydrogeol. J. (2016). https://doi.org/10.1007/s10040-016-1441-8
40. De Dreuzy, J.R., Davy, P., Bour, O.: Hydraulic properties of two-dimensional random fracture networks following a power law length distribution: 1. Effective connectivity. Water Resourc. Res. **37**(8), 2065–2078 (2001). https://doi.org/10.1029/2001WR900011
41. Darcel, C., Davy, P., Le Goc, R., Dreuzy, J.R.D., Bour, O.: Statistical methodology for discrete fracture model - including fracture size, orientation uncertainty together with intensity uncertainty and variability, (2009). Technical report
42. Tran, N.H.: Fracture orientation characterization: Minimizing statistical modelling errors. Comput. Stat. Data Anal. **51**(6), 3187–3196 (2007). https://doi.org/10.1016/J.CSDA.2006.10.024
43. Zhu, W., He, X., Lei, G., Wang, M.: Complexity analysis of three-dimensional stochastic discrete fracture networks with fractal and multifractal techniques. J. Struct. Geol. **162**, 104690 (2022). https://doi.org/10.1016/J.JSG.2022.104690
44. McKay, M.D., Beckman, R.J., Conover, W.J.: A comparison of three methods for selecting values of input variables in the analysis of output from a computer code. Technometrics **21**(2), 239 (1979). https://doi.org/10.2307/1268522
45. Kazemi, H.: Pressure transient analysis of naturally fractured reservoirs with uniform fracture distribution. Soc. Petrol. Eng. J. **9**(04), 451–462 (1969). https://doi.org/10.2118/2156-A
46. Matthäi, S.K., Belayneh, M.: Fluid flow partitioning between fractures and a permeable rock matrix. Geophys. Res. Lett. 31(7), (2004). https://doi.org/10.1029/2003GL019027
47. Kharrat, R., Ott, H.A., Kharrat, R., Ott, H.: A comprehensive review of fracture characterization and its impact on oil production in naturally fractured reservoirs. Energies **16**(8), 3437 (2023). https://doi.org/10.3390/EN16083437
48. Snow, D.T.: Rock fracture spacings, openings, and porosities. J. Soil Mech. Found. Div. **94**(1), 73–91 (1968). https://doi.org/10.1061/JSFEAQ.0001097
49. Olson, J.E.: Sublinear scaling of fracture aperture versus length: An exception or the rule? Journal of Geophysical Research: Solid Earth **108**(B9), (2003). https://doi.org/10.1029/2001JB000419
50. Shipton, Z.K., Evans, J.P., Robeson, K.R., Forster, C.B., Snelgrove, S.: Structural heterogeneity and permeability in faulted eolian sandstone: Implications for subsurface modeling of faults. AAPG Bull. **86**(5), 863–883 (2002). https://doi.org/10.1306/61EEDBC0-173E-11D7-8645000102C1865D
51. Li, J.Z., Laubach, S.E., Gale, J.F.W., Marrett, R.A.: Quantifying opening-mode fracture spatial organization in horizontal wellbore image logs, core and outcrop: Application to Upper Cretaceous Frontier Formation tight gas sandstones, USA. J. Struct. Geol. **108**, 137–156 (2018). https://doi.org/10.1016/J.JSG.2017.07.005
52. Knutson, C.F., Cox, D.O., Dooley, K.J., Sisson, J.B.: Characterization of low-permeability media using outcrop measurements. Proceedings - SPE Annual Technical Conference and Exhibition. Omega, 729–739 (1993). https://doi.org/10.2118/26487-MS
53. Cao, Y.B., Feng, X.T., Yan, E.C., Chen, G., Lü, F.f., Ji, H.b., Song, K.Y.: Calculation method and distribution characteristics of fracture hydraulic aperture from field experiments in fractured granite area. Rock Mech. Rock Eng. **49**(5), 1629–1647 (2015). https://doi.org/10.1007/S00603-015-0881-0
54. Hooker, J.N., Gale, J.F.W., Gomez, L.A., Laubach, S.E., Marrett, R., Reed, R.M.: Aperture-size scaling variations in a low-strain opening-mode fracture set, Cozzette Sandstone. Colorado. J. Struct. Geol. **31**(7), 707–718 (2009). https://doi.org/10.1016/J.JSG.2009.04.001
55. Miranda, T.S., Santos, R.F., Barbosa, J.A., Gomes, I.F., Alencar, M.L., Correia, O.J., Falcão, T.C., Gale, J.F.W., Neumann, V.H.: Quantifying aperture, spacing and fracture intensity in a carbonate reservoir analogue: Crato Formation, NE Brazil. Marine and Petroleum Geology, vol. 97, pp. 556–567. (2018). https://doi.org/10.1016/J.MARPETGEO.2018.07.019
56. Kamel Targhi, E., Bruna, P.-O., Daniilidis, A., Rongier, G., Geiger, S.: GeoDFN, a flexible, open-source software for generating geologically consistent discrete fracture networks. 4TU.ResearchData (2024). https://doi.org/10.4121/0dc9c47a-2294-4811-a0fe-e049cb15ff3d
57. Zeeb, C., Gomez-Rivas, E., Bons, P.D., Blum, P.: Evaluation of sampling methods for fracture network characterization using outcrops. AAPG Bull. **97**(9), 1545–1566 (2013). https://doi.org/10.1306/02131312042
58. Healy, D., Rizzo, R.E., Cornwell, D.G., Farrell, N.J.C., Watkins, H., Timms, N.E., Gomez-Rivas, E., Smith, M.: FracPaQ: A MATLAB^{TM} toolbox for the quantification of fracture patterns. J. Struct. Geol. **95**, 1–16 (2017). https://doi.org/10.1016/J.JSG.2016.12.003
59. Lie, K.A., Krogstad, S., Ligaarden, I.S., Natvig, J.R., Nilsen, H.M., Skaflestad, B.: Open-source MATLAB implementation of consistent discretisations on complex grids. Comput. Geosci. **16**(2), 297–322 (2012). https://doi.org/10.1007/S10596-011-9244-4/METRICS
60. Lie, K.-A.: An introduction to reservoir simulation using MATLAB/GNU octave: User guide for the MATLAB reservoir simulation toolbox (MRST). An Introduction to Reservoir Simulation Using MATLAB/GNU Octave. (2019). https://doi.org/10.1017/9781108591416

61. Tran, M., Jha, B.: Effect of poroelastic coupling and fracture dynamics on solute transport and geomechanical stability. Water Resour. Res. **57**(10), 2021–029584 (2021). https://doi.org/10.1029/2021WR029584
62. Xiang, Z., Zhen, R., Xu, Y., Wang, S., Ao, X., Chen, Z., Hu, J.: A numerical pressure transient model of fractured well with complex fractures of tight gas reservoirs considering gas-water two phase by EDFM. Geoenergy Sci. Eng. **231**(1), 212286 (2023). https://doi.org/10.1016/j.geoen.2023.212286
63. Fumagalli, A., Pasquale, L., Zonca, S., Micheletti, S.: An upscaling procedure for fractured reservoirs with embedded grids. Water Resour. Res. **52**(8), 6506–6525 (2016). https://doi.org/10.1002/2015WR017729
64. Wong, D.L.Y., Doster, F., Geiger, S., Kamp, A.: Partitioning thresholds in hybrid implicit-explicit representations of naturally fractured reservoirs. Water Resour. Res. **56**(2), 2019–025774 (2020). https://doi.org/10.1029/2019WR025774
65. Li, S., Kang, Z., Feng, X.T., Pan, Z., Huang, X., Zhang, D.: Three-dimensional hydrochemical model for dissolutional growth of fractures in karst aquifers. Water Resour. Res. **56**(3), 2019–025631 (2020). https://doi.org/10.1029/2019WR025631
66. Zhang, W., Han, D., Jiao, K., Chen, Y., Yuan, Q., Gong, L., Yu, B.: Research on the THMC Coupling Model for Enhanced Geothermal Systems Based on the Framework of EDFM. In: Mechanisms and Machine Science, vol. 145, pp. 963–978. Springer, (2024). https://doi.org/10.1007/978-3-031-42987-3-67
67. Wong, D.L.Y., Doster, F., Geiger, S.: Embedded Discrete Fracture Models. In: Lie, K.-A., Møyner, O. (eds.) Advanced Modeling with the MATLAB Reservoir Simulation Toolbox, pp. 375–408. Cambridge University Press (2021)
68. Narr, W., Suppe, J.: Joint spacing in sedimentary rocks. J. Struct. Geol. **13**(9), 1037–1048 (1991). https://doi.org/10.1016/0191-8141(91)90055-N
69. Narr, W., Schechter, D., Thompson, L.: Naturally Fractured Reservoir Characterization/ by Wayne Narr, David W. Schechter and Laird B. Thompson, p. 115. Society of Petroleum Engineers, (2006)
70. Liu, R., Li, B., Jiang, Y., Yu, L.: A numerical approach for assessing effects of shear on equivalent permeability and nonlinear flow characteristics of 2-D fracture networks. Adv. Water Resour. **111**, 289–300 (2018). https://doi.org/10.1016/J.ADVWATRES.2017.11.022
71. Petitjean, F., Ketterlin, A., Gançarski, P.: A global averaging method for dynamic time warping, with applications to clustering. Pattern Recogn. **44**(3), 678–693 (2011). https://doi.org/10.1016/J.PATCOG.2010.09.013
72. Sakoe, H., Chiba, S.: Dynamic Programming Algorithm Optimization for Spoken Word Recognition. IEEE Trans. Acoust. Speech Signal Process. **26**(1), 43–49 (1978). https://doi.org/10.1109/TASSP.1978.1163055
73. Ratanamahatana, C.A., Keogh, E.: Making time-series classification more accurate using learned constraints. In: Proceedings of the 2004 SIAM International Conference on Data Mining, pp. 11–22. Society for Industrial and Applied Mathematics Publications, (2004). https://doi.org/10.1137/1.9781611972740.2
74. Kaufman, L., Rousseeuw, P.: Finding Groups in Data: an Introduction to Cluster Analysis, Wiley (2009)
75. Liao, T.W.: Clustering of time series data– a survey. Pattern Recogn. **38**(11), 1857–1874 (2005). https://doi.org/10.1016/J.PATCOG.2005.01.025
76. Paparrizos, J., Yang, F., Li, H.: Bridging the Gap: A Decade Review of Time-Series Clustering Methods, (2024)
77. Rousseeuw, P.J.: Silhouettes: A graphical aid to the interpretation and validation of cluster analysis. J. Comput. Appl. Math. **20**(C), 53–65 (1987). https://doi.org/10.1016/0377-0427(87)90125-7
78. Kruskal, J.B.: Nonmetric multidimensional scaling: A numerical method. Psychometrika **29**(2), 115–129 (1964). https://doi.org/10.1007/BF02289694
79. Torgerson, W.S.: Multidimensional scaling: I. Theory and method. Psychometrika **17**(4), 401–419 (1952). https://doi.org/10.1007/BF02288916
80. Davies, D.L., Bouldin, D.W.: A cluster separation measure. IEEE Trans. Pattern Anal. Mach. Intell. PAMI **1**(2), 224–227 (1979). https://doi.org/10.1109/TPAMI.1979.4766909
81. Caliñski, T., Harabasz, J.: A dendrite method for cluster analysis. Commun. Stat. Theory Methods **3**(1), 1–27 (1974). https://doi.org/10.1080/03610927408827101
82. Aldrich, G., Hyman, J.D., Karra, S., Gable, C.W., Makedonska, N., Viswanathan, H., Woodring, J., Hamann, B.: Analysis and visualization of discrete fracture networks using a flow topology graph. IEEE Trans. Visual Comput. Graphics **23**(8), 1896–1909 (2017). https://doi.org/10.1109/TVCG.2016.2582174
83. Breiman, L.: Random forests. Mach. Learn. **45**(1), 5–32 (2001). https://doi.org/10.1023/A:1010933404324/METRICS
84. Lundberg, S.M., Allen, P.G., Lee, S.-I.: A unified approach to interpreting model predictions. In: Advances in Neural Information Processing Systems, p. 30. (2017)
85. Riehmann, P., Hanfler, M., Froehlich, B.: Interactive sankey diagrams. In: Proceedings - IEEE Symposium on Information Visualization, INFO VIS, pp. 233–240. (2005). https://doi.org/10.1109/INFVIS.2005.1532152
86. Valys, B.: Time-series clustering and visualization for insights into multimorbidity progression, University of Sheffield (2025). (PhD thesis)
87. Al-Ahmadi, H.A., Wattenbarger, R.A.: Triple-porosity Models: One Further Step Towards Capturing Fractured Reservoirs Heterogeneity. Society of Petroleum Engineers - SPE/DGS Saudi Arabia Section Technical Symposium and Exhibition 2011, 1155–1175 (2011). https://doi.org/10.2118/149054-MS

88. Liu, H., Liao, X., Tang, X., Chen, Z., Zhao, X., Zou, J.D.: A well test model based on embedded discrete-fracture method for pressure-transient analysis of fractured wells with complex fracture networks. J. Petrol. Sci. Eng. **196**, 108042 (2021). https://doi.org/10.1016/J.PETROL.2020.108042
89. Wang, Z., Li, W., Qiao, L., Liu, J., Yang, J.: Hydraulic properties of fractured rock mass with correlated fracture length and aperture in both radial and unidirectional flow configurations. Comput. Geotech. **104**, 167–184 (2018). https://doi.org/10.1016/J.COMPGEO.2018.08.017

Authors and Affiliations

Elahe Kamel Targhi[1] · Guillaume Rongier[1] · Pierre-Olivier Bruna[1] · Alexandros Daniilidis[1] · Sebastian Geiger[1]

✉ Elahe Kamel Targhi
e.kameltarghi@tudelft.nl

Guillaume Rongier
g.rongier@tudelft.nl

Pierre-Olivier Bruna
p.b.r.bruna@tudelft.nl

Alexandros Daniilidis
a.daniilidis@tudelft.nl

Sebastian Geiger
s.geiger@tudelft.nl

[1] Department of Geoscience and Engineering, Delft University of Technology, Stevinweg 1, Delft 2628CN, Zuid-Holland, The Netherlands